

Article

Satellite Retrievals of *Karenia brevis* Harmful Algal Blooms in the West Florida Shelf Using Neural Networks and Comparisons with Other Techniques

Ahmed El-habashi ^{1,†}, Ioannis Ioannou ^{2,†}, Michelle C. Tomlinson ^{3,†}, Richard P. Stumpf ^{3,†} and Sam Ahmed ^{1,*,†}

¹ The City College of New York, Optical Remote Sensing Laboratory, Department of Electrical Engineering, 160 Convent Ave, New York, NY 10031, USA; aelhaba00@citymail.cuny.edu

² NATO Science & Technology Organization, Center for Maritime Research and Experimentation, Viale San, Bartolomeo 400, La Spezia 19126, Italy; yannismail@gmail.com

³ NOAA National Centers for Coastal Ocean Science, 1305 East-West Highway Code N/SCI1 Silver Spring, MD 20910, USA; michelle.tomlinson@noaa.gov (M.C.T.); richard.stumpf@noaa.gov (R.P.S.)

* Correspondence: ahmed@ccny.cuny.edu; Tel.: +1-212-650-7250; Fax: +1-212-650-8249

† These authors contributed equally to this work.

Academic Editors: Deepak R. Mishra, Richard W. Gould Jr., Xiaofeng Li and Prasad S. Thenkabail

Received: 30 December 2015; Accepted: 20 April 2016; Published: 4 May 2016

Abstract: We describe the application of a Neural Network (NN) previously developed by us, to the detection and tracking, of *Karenia brevis* Harmful Algal Blooms (KB HABs) that plague the coasts of the West Florida Shelf (WFS) using Visible Infrared Imaging Radiometer Suite (VIIRS) satellite observations. Previous approaches for the detection of KB HABs in the WFS primarily used observations from the Moderate Resolution Imaging Spectroradiometer Aqua (MODIS-A) satellite. They depended on the remote sensing reflectance signal at the 678 nm chlorophyll fluorescence band (R_{rs678}) needed for both the normalized fluorescence height (nFLH) and Red Band Difference algorithms (RBD) currently used. VIIRS which has replaced MODIS-A, unfortunately does not have a 678 nm fluorescence channel so we customized the NN approach to retrieve phytoplankton absorption at 443 nm (a_{ph443}) using only R_{rs} measurements from existing VIIRS channels at 486, 551 and 671 nm. The a_{ph443} values in these retrieved VIIRS images, can in turn be correlated to chlorophyll-*a* concentrations [*Chla*] and KB cell counts. To retrieve KB values, the VIIRS NN retrieved a_{ph443} images are filtered by applying limiting constraints, defined by (i) low backscatter at R_{rs} 551 nm and (ii) a minimum a_{ph443} value known to be associated with KB HABs in the WFS. The resulting filtered residual images, are then used to delineate and quantify the existing KB HABs. Comparisons with KB HABs satellite retrievals obtained using other techniques, including nFLH, as well as with *in situ* measurements reported over a four year period, confirm the viability of the NN technique, when combined with the filtering constraints devised, for effective detection of KB HABs.

Keywords: neural networks; harmful algal blooms; ocean color remote sensing reflectance; *Karenia brevis*; retrieved chlorophyll-*a*; normalized fluorescence height; West Florida Shelf

1. Introduction

A new approach is needed for the detection and tracking of KB HABs that frequently plague the coasts and beaches of the West Florida Shelf (WFS) using VIIRS satellite data. Such a monitoring capability for KB HABs is important because of their negative impacts on ecology and health. More specifically, high KB HABs levels pose a threat to fisheries and human health, and directly affect tourism and local economies [1]. Effective KB HABs detection and tracking approaches are needed for use with VIIRS so that NOAA can extend its HABs monitoring capabilities, which previously relied on

MODIS-A imagery [2–11]. Unfortunately, VIIRS, unlike its predecessor MODIS-A, does not have a 678 nm channel to detect chlorophyll fluorescence, which is used in the normalized fluorescence height (nFLH) algorithm [7,8], or in the Red Band Difference (RBD) algorithm, developed by our CCNY group [5,6]. Both of these techniques have demonstrated that the *Rrs* 678 nm from the MODIS-A fluorescence band helps in effectively detecting and tracking *KB* HABs in the WFS [3–8]. To overcome the lack of a fluorescence channel on VIIRS, the alternative approach described here, bypasses the need for measurements of chlorophyll fluorescence, allowing us to extend *KB* HABs satellite monitoring capabilities in the WFS to VIIRS.

The essence of the approach is the application of a standard multiband neural network (NN) inversion algorithm, previously developed and reported by us [12–15], that takes VIIRS *Rrs* measurements at the 486, 551 and 671 nm bands (or 488, 555, and 667 nm for MODIS-A) as inputs, and produces as output the related Inherent Optical Properties (IOPs), namely: absorption coefficients of phytoplankton (a_{ph443}) dissolved organic matter (a_g) and non-algal particulates (a_{dm}) as well as the particulate backscatter coefficient, (bb_p) all at 443 nm. In this work, however, it is only with the NN output of a_{ph443} that we are concerned with and which can be converted to equivalent [*Chla*] using empirical relationships for specific absorption in the WFS which have been determined from *in situ* measurements [16]. For the next step, to obtain *KB* values from the VIIRS NN retrieved a_{ph443} image, we apply additional constraints, defined by (i) low backscatter manifested as a maximum *Rrs*551 value and (ii) a minimum [*Chla*] threshold [4,17,18] (and hence an equivalent minimum $a_{ph443min}$ value) both known to be associated with *KB* HABs in the WFS. These two constraining filter processes are applied sequentially to the VIIRS NN retrieved a_{ph443} image. First an image is made of retrieved VIIRS *Rrs*551. A mask is then made of all pixels with $Rrs551 \geq Rrs551max$, the maximum value known to be compatible with the existence *KB* HABs. This mask is then applied, in a filter process hereinafter dubbed F1, to the VIIRS NN retrieved a_{ph443} image to exclude pixels with $Rrs551 \geq Rrs551max$. The residual image, after application of filter process F1, will only show a_{ph443} values that also comply with $Rrs551 \leq Rrs551max$. Then, in a second filter process, hereinafter dubbed F2, all values of $a_{ph443} \leq a_{ph443min}$ are eliminated. The residual image will now only show a_{ph443} values that are compatible with both criteria for *KB* HABs, and are therefore representative of *KB* HABs.

It will be shown that when both these filter condition are applied to VIIRS NN a_{ph443} retrievals, they can be used to effectively delineate and quantify *KB* HABs in the WFS. The *KB* HABs retrieved in this manner also show good correlations with *in situ* *KB* HABs measurements as well as with nFLH retrievals and other techniques to which the same filtering criteria have been applied, confirming the viability of the approach.

2. Materials and Methods

Neural Network Algorithm Background

In the work presented here, we use our synthetically trained NN algorithm [12–15] to solve the inverse problem [19,20] of retrieving physical variables, including a_{ph443} , from VIIRS observations of *Rrs* at 486, 551 and 671 nm in the WFS. A brief background summary is given here. Additional details are available in the cited references and in the Appendix. The latter also gives the necessary parameters for using the NN with a MATLAB tool for satellite retrievals by any interested reader. As mentioned in the introduction, we use a standard multiband NN inversion algorithm that takes VIIRS *Rrs* measurements at the 486, 551 and 671 nm bands as inputs, and produces as outputs the related IOPs, namely: a_{ph443} , a_g and a_{dm} as well as bb_p , all at 443 nm. (As mentioned earlier, it is only with the a_{ph443} output of NN that we are concerned with here).

Synthetic Dataset

For development of the algorithm, available measurement data from the NASA Bio-Optical Marine Algorithm Data set [21], (NOMAD) was used as a basis for establishing a range of possible

IOP parameters and examining potential relationships between them. The full range of parameters, applicable to both oceanic and coastal waters, and the relationships established between them were used as inputs to a bio-optical model [14,22,23]. The range and variability of IOPs used in our bio-optical modeling is well represented in the literature [22–35]. Our model, as illustrated in Figure 1a, has four components: water, phytoplankton, colored dissolved organic matter (CDOM) and non-algal particulates (NAP) as inputs to create a synthetic data base consisting of 20,000 IOP combinations covering the entire observable range of possible IOP parameters. These IOPs were then used with a HydroLight based [36], parameterized forward model, described in Lee 2002 [23] to generate corresponding sets of Rrs values at 486, 551 and 671 nm for VIIRS, and at 488, 555 and 667 nm for MODIS-A, associated with each of the 20,000 IOPs (and the related different combinations of the four components) [12–15].

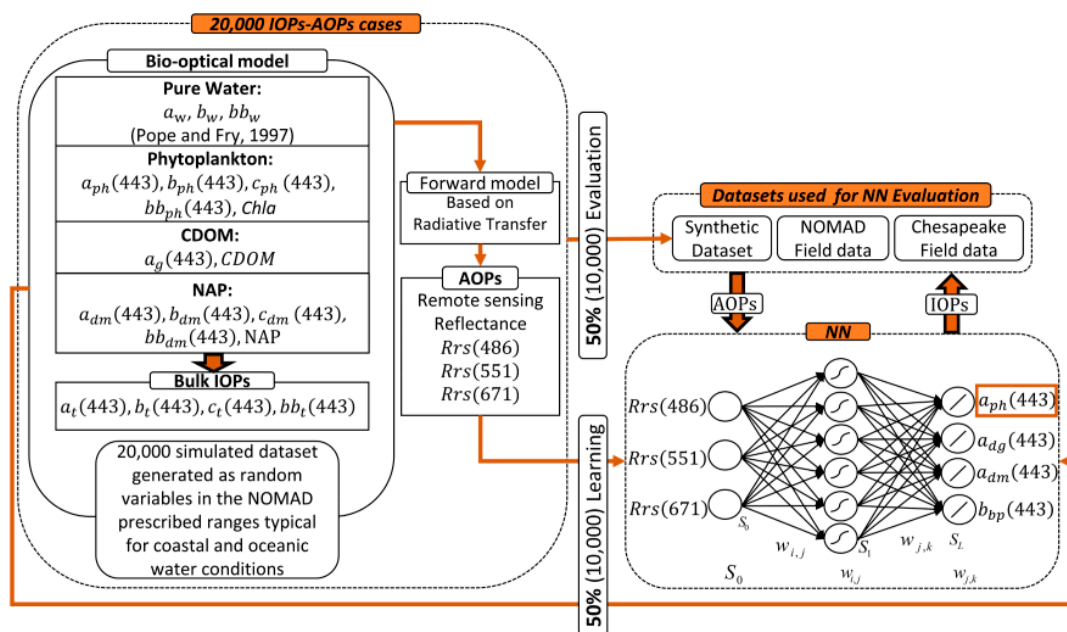


Figure 1. (a) Flowchart of Bio-Optical model and the Forward Model simulations; (b) Architecture of VIIRS NN, one-hidden layer multilayer perceptron (MLP), trained with 10,000 set of Rrs and related IOPs.

Algorithm Training

Once the comprehensive set of Rrs spectral channel data together with the associated IOP's are assembled, a robust NN can be developed to connect the Rrs directly to the physical parameter to be retrieved. As is standard, a subset of the data is used to train the underlying NN and the rest used for validations. In our case, 50% (10,000) of these sets of Rrs and related IOPs were used [12–15] to train the NN model to obtain the relationship between input Rrs values at the 486, 551 and 671 nm bands for VIIRS and the output $a_{ph}, a_g, a_{dm}, bb_p$ coefficients at 443 nm, which is at the peak of phytoplankton absorption spectrum, and thus exhibits the most sensitive variation in natural waters (and where a_g and a_d are mutually constrained through an empirically derived relationship based on a study of NOMAD [21] values). Figure 1b shows the VIIRS NN Architecture used. In our implementation, it was found that a one-hidden-layer multilayer perceptron (MLP-NN) with six neurons at the hidden layer was able to model our problems well. Since this architecture appeared appropriate for our needs, we did not further explore how this relationship might be improved by increasing the number of neurons or layers.

The VIIRS NN algorithm was tested and evaluated using multiple experiments. It was (a) tested initially on half the simulated data set that was not used in the training (b) field data from the,

(NOMAD) and (c) data from our own field campaign in the Chesapeake Bay during 2013, which represents well the typical range of water optical properties and chlorophyll-*a* concentrations in coastal regions. These tests confirmed good retrievals of a_{ph443} by the NN [13,14] and provided strong motivation for its use in the current work. The results of the present work have further confirmed its viability for effective retrievals of a_{ph443} in the coastal waters of the WFS from VIIRS measurements at the 486, 551 and 671 nm bands. In this context, we would also add that though we are estimating a_{ph443} at 443 nm, the Rrs values used as inputs to the NN to retrieve it are at longer wavelengths, 486, 551 and 671 nm, and do not require measurements at the shorter wavelength channels, M1 (415 nm) and M2 (443 nm) which are typically most impacted by atmospheric correction difficulties.

As mentioned above, a more detailed description of the NN, and its background are given in the Appendix. The parameters needed for its implementation and the retrieval a_{ph443} from inputs of Rrs 486, 551 and 671 nm. The related calculations that can be readily performed by interested readers using a MATLAB script are also described in the Appendix. We would be interested to hear the results of other retrievals, particularly for other areas where *KB* HABs are known to exist.

3. Results and Discussion

3.1. VIIRS Retrievals of $Rrs551$ and a_{ph443} and Determination of Limiting Values of $Rrs551_{max}$ and $a_{ph443_{min}}$ in a *KB* Bloom Environment

Figure 2 shows *KB* cell counts associated with a prominent *KB* HAB bloom in the WFS with its peak occurring around 2 September 2014. This bloom has been extensively studied [7,8,15]. Figure 2, from the NOAA HABSOS site [37] shows the bloom area with indicators (circles of different sizes) for *KB* HABs cell counts for concurrent or near concurrent dates over the period (27 August–17 September 2014). Figure 3a shows VIIRS retrievals of $Rrs551$ for 2 September 2014 and for the same location. It shows, overlaid, the cell count information from Figure 2. Considering backscatter data as a *KB* indicator, Refs. [3,17,18] give maximum permissible values of backscatter, compatible with *KB* HABs, as $bb_{p550} \leq 0.0045 \text{ m}^2 \cdot \text{mg}^{-1}$ at 550 nm. In addition, for Rrs 551 which is taken to serve as a proxy for backscatter, the equivalent max permissible value is $Rrs551 \leq 7.0 \times 10^{-3} \text{ sr}^{-1}$. However, by inspection of Figure 3a of retrieved [38] and *in situ* [37] values we concluded that a value of approximately $Rrs551 \leq 6.0 \times 10^{-3} \text{ sr}^{-1}$ appears more appropriate as the highest permissible limiting value for compatibility with *KB* HABs. If that value is applied to Figure 3a, as filter process F1, all pixels with $Rrs551 \geq 6.0 \times 10^{-3} \text{ sr}^{-1}$ are screened out, leaving the residual pixels in Figure 3b as compatible with *KB* HABs as far as backscatter is concerned.

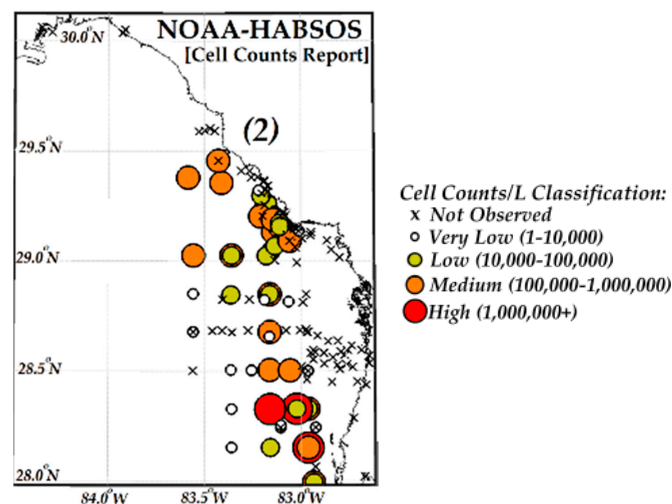


Figure 2. NOAA HABSOS data [37] with *in situ* *KB* concentrations, for period 8 August–17 September 2014.

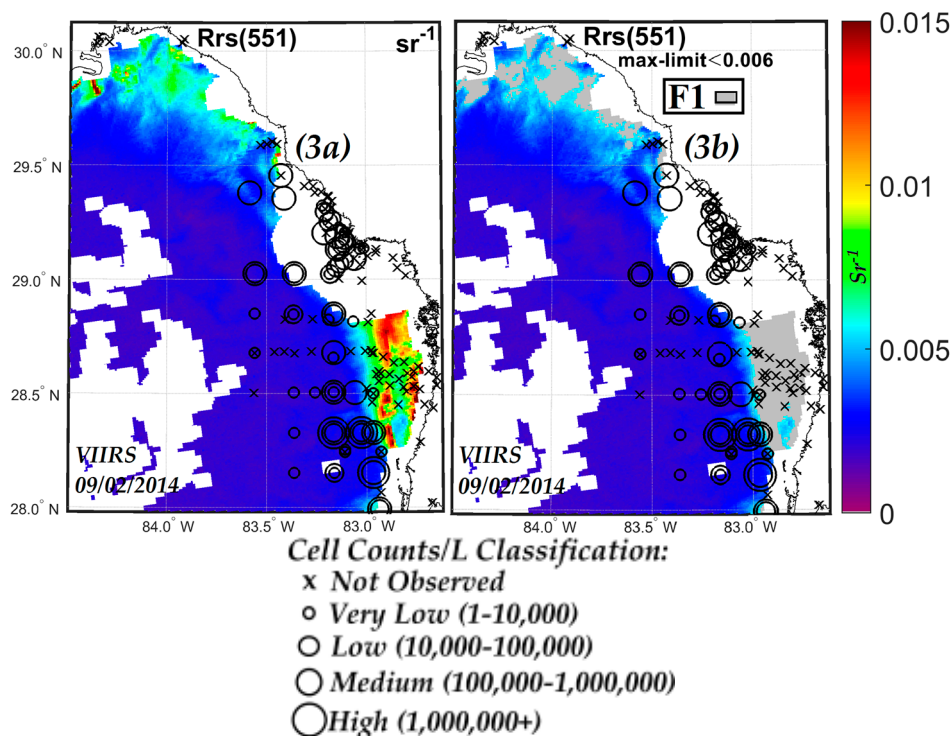


Figure 3. (a) VIIRS Rrs_{551} image; (b) Residual Rrs_{551} image after F1 mask (dark grey) is applied showing residual $\{Rrs_{551} \leq 0.006 \text{ sr}^{-1}\}$. Note that these images are overlaid with NOAA-HABSOS KB Cell Counts, from Figure 2 above. White areas represent cloud cover or invalid data.

We next apply the pixel mask shown in Figure 3b, resulting from application of Filter 1 conditions to VIIRS Rrs_{551} retrievals, to Figure 4a which shows a_{ph443} retrieved by the NN for the same 2 September 2014 date and location. This process eliminates all a_{ph443} values in Figure 4a that do not satisfy $Rrs_{551} \leq 6.0 \times 10^{-3} \text{ sr}^{-1}$ requirements for compatibility with KB HABs. The residual values, shown in Figure 3b satisfy the Rrs_{551} limit requirements. Cell counts from Figure 2 are again shown overlaid in Figure 4b.

We next examine the appropriate F2 filter values for minimum a_{ph443} consistent with KB HABs. Now Refs. [17,18] give the minimum $[Chla]$ concentration compatible with KB HABs in the WFS as $[Chla] \geq 1.5 \mu\text{g} \cdot \text{L}^{-1}$. This is converted into equivalent a_{ph443} using the empirical relationship [16]:

$$a_{ph443} = 0.051 \times [Chla]^{0.74}, m^{-1} \quad (1)$$

Which gives $a_{ph443} \geq 0.0688 \text{ m}^{-3}$ as the minimum permissible value. Again, by inspection of Figure 4b against overlaid *in situ* values, we conclude that a value of approximately $a_{ph443} \geq 0.061 \text{ m}^{-3}$ is more appropriate as the limiting value for compatibility with KB HABs.

Applying this value as Filter F2 to Figure 4b we eliminate pixels that are not compatible with KB and end up with Figure 5a. This shows only residual values with $a_{ph443} \geq 0.061 \text{ m}^{-3}$ which also satisfy $Rrs_{551} < 6.0 \times 10^{-3} \text{ sr}^{-1}$. These are therefore residual values compatible with and representative of KB HABs. Comparison of the residual a_{ph443} (left hand scale) and equivalent $[Chla]$ (right hand scale) in Figure 5a, which represent the retrieved KB HABs values, show good qualitative agreement with the KB HABs cell counts in Figure 2.

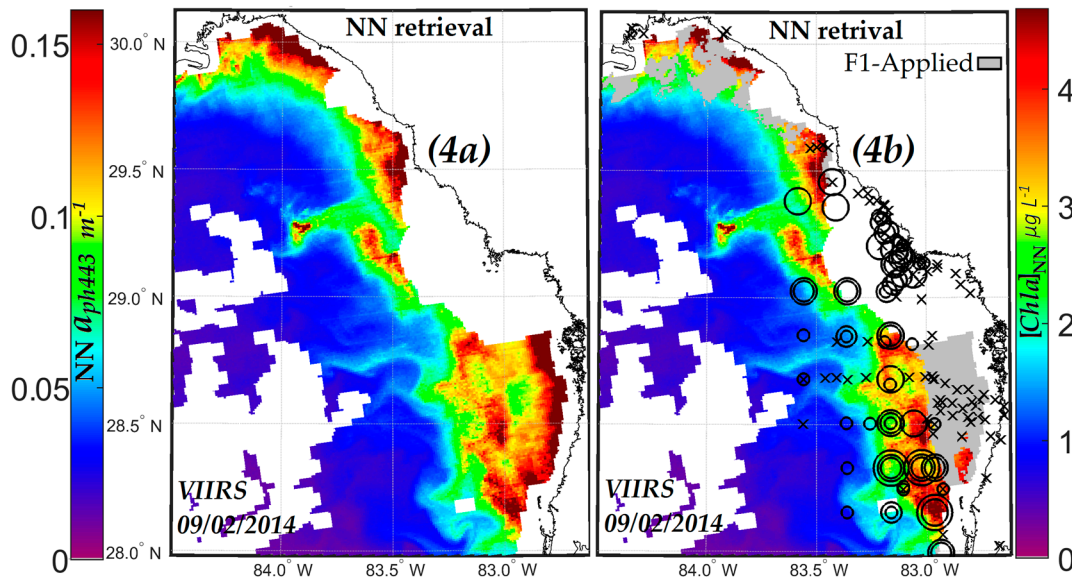


Figure 4. (a) Shows retrieved NN a_{ph443} (left hand scale) and NN equiv. [Chla] (right hand scale); (b) Same image with F1 mask applied. Cell counts classifications same for Figure 2, Figure 3a,b, and Figure 4b. Dark gray represents F1 mask and white areas represent cloud cover or invalid data.

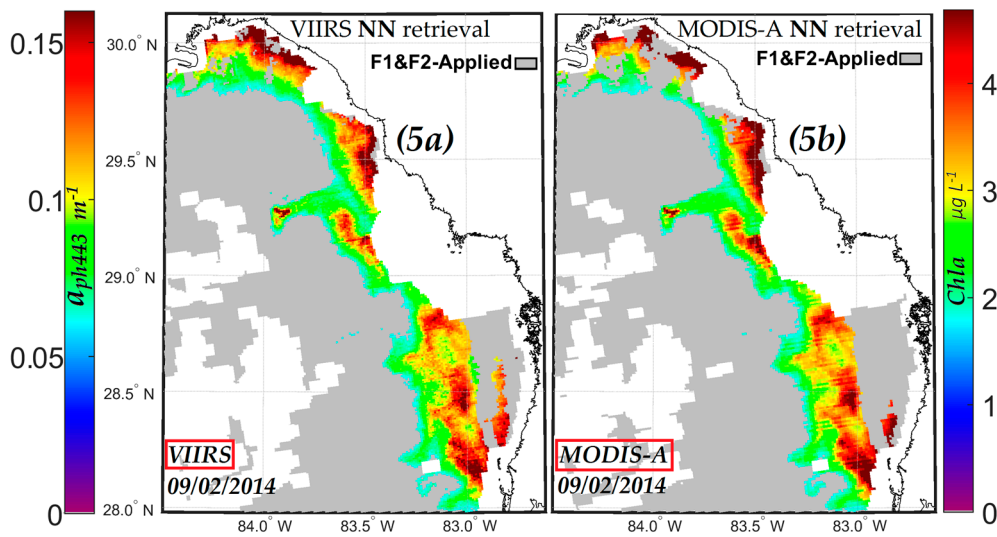


Figure 5. (a) Shows VIIRS retrieved NN a_{ph443} (left hand scale) and equiv. [Chla] (right hand scale) after filter process masks F1 and F2 are applied. These residual values are therefore compatible with and show the extent of the KB blooms; (b) MODIS-A NN retrieved a_{ph443} (left hand scale) and equiv. [Chla] (right hand scale) after filter process masks F1 and F2 are applied. Residual values are therefore compatible with and indicate KB blooms. Dark gray represents F1&F2 masks and white represents cloud cover or invalid data.

3.2. Comparisons of NN KB HABs with Other Retrieval Techniques

We next compare the NN retrievals of KB HABs, described in the last section, with retrievals using other techniques. In doing so, it is not the intention to present an exhaustive comparison of the many approaches that have been studied for the detection of KB HABs in the WFS. Some of these are listed in [2–11]. For more details, the reader is referred to recent excellent surveys and comparisons in [3,11]. We focus here, instead, on comparisons with three distinct categories of retrieval techniques.

The existing satellite algorithms that are relevant to the detection of *KB* HABs in the WFS rely on retrieved chlorophyll-*a* concentrations [*Chla*] as part of their processing. They retrieve it primarily in one of three ways: (i) using the remote sensing reflectance fluorescence signal at *Rrs*678 measured by the MODIS-A satellite; and (ii) using blue-green ratio algorithms, exemplified by the NASA OC3 and OCI products [21,39–41]; and (iii) a more recent WFS region specific empirical algorithm, the Red Green chlorophyll-*a* Index (RGCI) which retrieves [*Chla*] using 2 visible VIIRS or MODIS-A bands [42]. Those methods (i) using the 678 nm fluorescence signal, include the normalized fluorescence height (nFLH) [2–11] and Red Band Difference (RBD) techniques [5,6]. (nFLH is FLH normalized to solar radiance); Those methods (ii) using blue-green ratio algorithms, include the chlorophyll-*a* anomaly technique and related approaches [43–52]. The method using RGCI, has been modified very recently, and has been reported for [*Chla*] retrievals but has not yet been applied to *KB* retrievals [42].

Amongst the various available *KB* HABs retrieval techniques that have been comprehensively evaluated, nFLH and RBD exhibited the best *KB* HABs retrieval statistics [3] for the WFS. Accordingly, our paper focuses on comparisons of NN retrievals against retrievals using (i) nFLH/RBD fluorescence and (ii) OCI/OC3 approaches; and (iii) RGCI approaches. These are each described in Sections 3.2.1–3.2.4 respectively, with detailed descriptions available in references [2–11,42–53].

3.2.1. Comparison of NN *KB* HABs Retrieval Techniques with Those Using the Normalized Fluorescence Height (nFLH) and Red Band Difference (RBD) Techniques

Both nFLH and RBD techniques use the magnitude of *Rrs* at the 678 nm fluorescence band relative to the values at adjacent bands on MODIS-A to detect the chlorophyll fluorescence [54] and [*Chla*] [55]. This approach, when coupled with the known low backscatter properties of *KB*, has been shown to help in effectively detecting *KB* in the WFS [3,17,18].

Since the nFLH technique requires the fluorescence signal at 678 nm, which is absent from VIIRS, comparisons of nFLH with the NN technique must be made using MODIS-A neural network retrievals. For this purpose, the same approach used with VIIRS NN (above) is used to obtain MODIS-A NN a_{ph443} retrievals. For MODIS-A, the *Rrs* values at the 488, 555 and 667 nm bands are used as inputs to the NN. For application of the F1 filter process, *Rrs* 555 nm is used as the proxy for backscatter (instead of the *Rrs* 551 nm used with VIIRS). The same F1 and F2 filter processes, with the same limiting values of $Rrs_{555} \leq 6.0 \times 10^{-3} \text{ sr}^{-1}$ for F1, and $a_{ph443} \geq 0.061 \text{ m}^{-3}$ for F2, were applied to MODIS-A NN retrievals for the same 2 September 2014 bloom date, to obtain *KB* compatible residual retrieval values. Figure 5b shows the MODIS-A NN retrieved a_{ph443} (left hand scale) and the equivalent [*Chla*] (right hand scale), after application of F1 and F2 filters. As can be seen, Figure 5b shows good qualitative agreement with Figure 5a from VIIRS NN retrievals.

We next compare the nFLH NASA product available [54] with MODIS-A for retrievals of nFLH values for the same 2 September 2014 WFS bloom. nFLH uses the height of the *Rrs* 678 nm (over a baseline connecting adjacent *Rrs* values) as an indicator of chlorophyll fluorescence magnitude [54,55]. Retrieved values are shown in Figure 6a. The left hand scale shows the nFLH NASA product, while the right hand scale shows the equivalent [*Chla*] value, converted using the empirical relationship [7]:

$$[Chla] = 1.255 \times (FLH \times 10)^{0.86}, \mu\text{gL}^{-1} \quad (2)$$

Figure 6b shows the same nFLH retrievals, but with filters F1 and F2 applied, *i.e.*, with the same pixels filtered out as in the MODIS-A NN retrievals in Figure 5b. It can be seen that Figure 6b shows good qualitative agreement with the images of Figure 5a,b.

For more quantitative comparisons, Figure 7a shows the correlation between equivalent [*Chla*] derived from nFLH in Figure 6a, against the retrieved MODIS-A NN derived equivalent [*Chla*]. To avoid complications from more complex waters in-shore areas, the comparison is made for the off-shore area A, shown demarcated in Figure 6a,b above. Without the *KB* compatibility filters applied, a high correlation, $R^2 = 0.87$ is obtained. With the F1 and F2 filters applied (eliminating non *KB* compatible pixels) the correlation becomes $R^2 = 0.71$, Figure 7b. The color coding of the dots in

Figure 7a,b indicates distance from shore, with red being the closest. As can be seen the spread gets larger closer to the shore, where waters are more complex and the uncertainty increases.

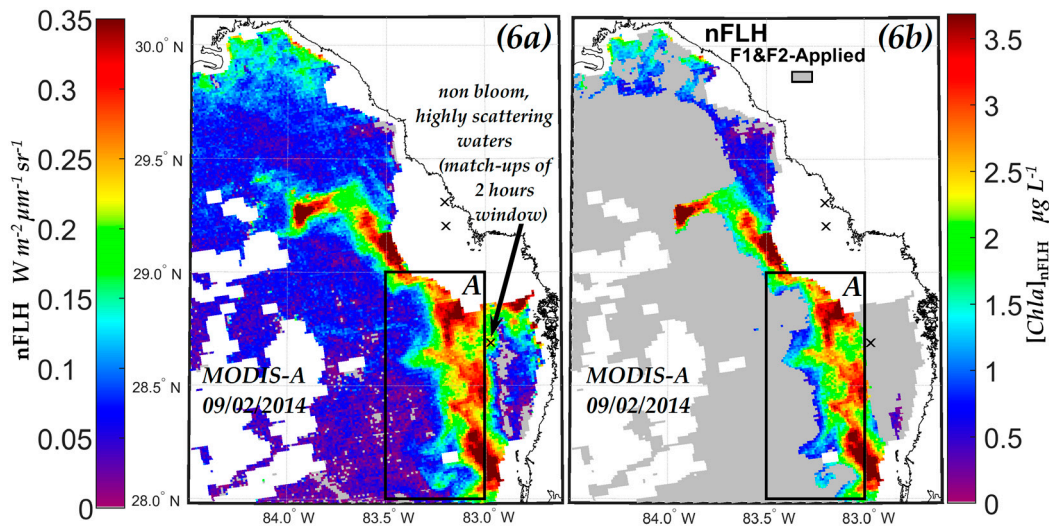


Figure 6. (a) MODIS-A nFLH (left hand scale) standard ocean color product, and equiv. [Chla] (right hand scale); (b) Same image as Figure 6a after filter process masks F1 and F2 are applied. Residual values are therefore compatible with and indicate KB blooms. Notes that “x” symbol in both images indicates no cell counts observed, *in situ* within 2 h windows from MODIS-A observation. Dark gray represents F1&F2 masks and white represent cloud cover or invalid data.

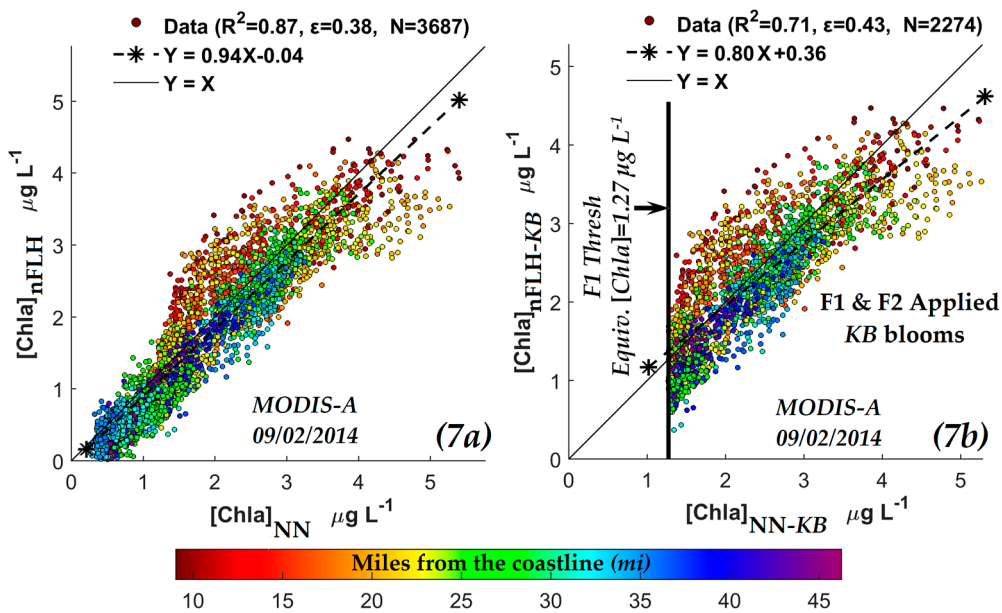


Figure 7. (a) MODIS-A nFLH equiv. [Chla] retrievals against MODIS-A NN equiv. [Chla] retrievals; (b) Shows the same retrievals as 5a but with F1 and F2 masks applied. Color coding of the dots denotes distance to shore, with red being the closest.

When the comparison between nFLH and VIIRS NN retrieved [Chla] is expanded beyond area A to include all areas, including the more complex in-shore waters, the correlation between them drops drastically, to $R^2 = 0.19$, shown in Figure 8. This may be due to the poor retrievals associated with nFLH for in-shore areas, where increased backscatter can cause an apparent increase in the red-near infrared spectral peak, increasing the apparent nFLH chlorophyll fluorescence signal, but which is in

fact only partially associated with the fluorescence peak [3,53,55,56]. Additional comparisons of nFLH and VIIRS NN in-shore retrievals are needed before more definitive conclusions can be arrived at.

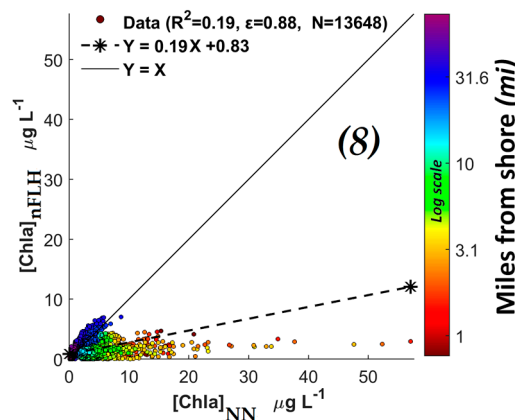


Figure 8. Retrieved MODIS-A nFLH [Chla] against retrieved MODIS-A NN [Chla], not restricted to open ocean area A, and includes in-shore areas. Color coding of the dots denotes distance to shore, with red being the closest. Note that color bar is in log scale.

3.2.2. Comparisons of MODIS-A NN Retrievals with Red Band Difference (RBD) Index Retrievals

We also examined retrievals from MODIS-A using the RBD index which is an empirical index previously developed by our CCNY group [5,6] often used in conjunction with the nFLH technique to confirm presence of KB blooms. The RBD index is defined by:

$$RBD = nLw(678) - nLw(667), W \cdot m^{-2} \cdot \mu m \cdot sr^{-1}$$

Figure 9 shows the RBD index, as defined above, retrieved from MODIS-A observations for the 2 September 2014 bloom, with filters F1 and F2 applied. As can be seen, this shows good qualitative agreement with both nFLH, MODIS-A NN [Chla], and HABSOS *in situ* images, Figures 2, 5b and 6b. As mentioned above, RBD, along with nFLH, has exhibited the best statistics for KB HABs retrievals [3].

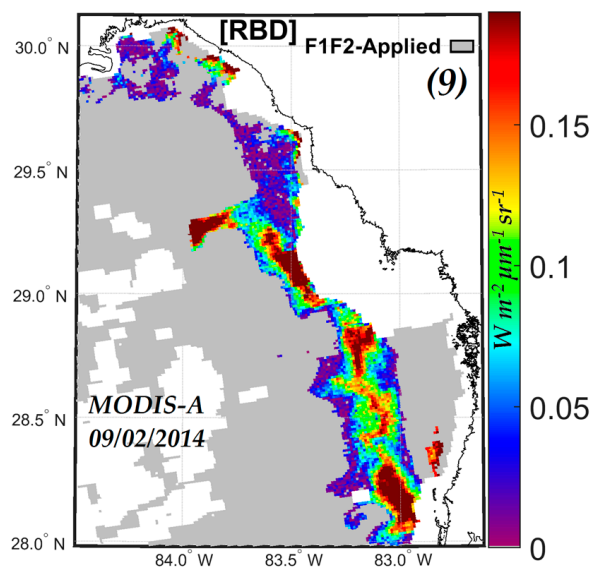


Figure 9. MODIS-A RBD retrieval after filter process masks F1 and F2 are applied, showing KB blooms. Dark gray represents F1&F2 masks and white represent cloud cover or invalid data.

3.2.3. Comparisons of VIIRS NN Retrievals with VIIRS Ocean Color Chlorophyll-*a* (OCI/OC3) Retrievals

We also compared the NN retrievals from VIIRS with retrievals using the OCI/OC3 indexes, both NASA products [53] for the same 2 September 2014 bloom. OCI and the related OC3 NASA products are [*Chla*] retrieval algorithms that make use of the ratio of blue/green bands in the MODIS-A and VIIRS satellites [21,39–41], and were found to yield exactly the same retrievals for our WFS conditions.

Correlations between VIIRS OCI/OC3 [*Chla*] and VIIRS NN equivalent [*Chla*] retrievals are shown in Figure 10a for the 2 September 2014 bloom for the off-shore area A. Without filter applications, $R^2 = 0.9$. When filters F1 and F2 are applied, the residual values consistent with KB HABs show, Figure 10b, a correlation of $R^2 = 0.78$. Figure 10c shows a comparison for area A of nFLH equivalent [*Chla*] retrievals against OCI/OC3 [*Chla*] retrievals with an $R^2 = 0.75$ without filters. Figure 10d shows $R^2 = 0.50$ with filters F1 and F2 applied, considerably lower than the correlation $R^2 = 0.71$, Figure 7b, between nFLH equivalent [*Chla*] versus NN equivalent [*Chla*].

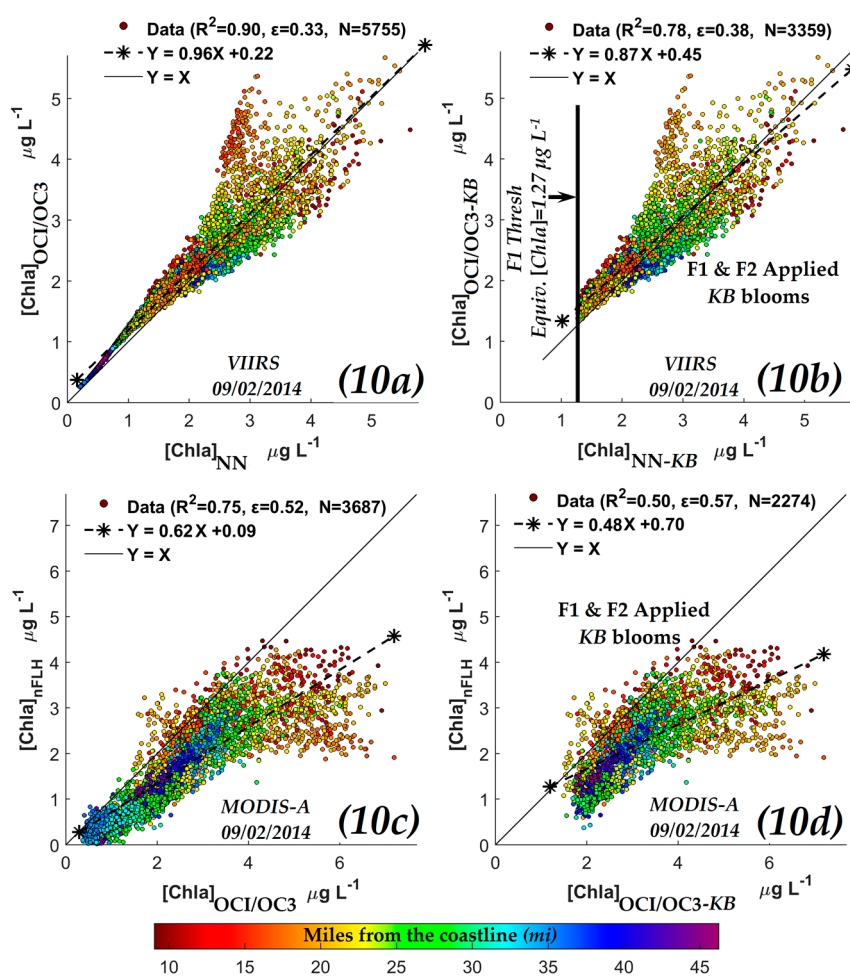


Figure 10. (a) Retrieved VIIRS OCI/OC3 [*Chla*] against retrieved MODIS-A NN [*Chla*]; (b) Same retrieval as 10a with Filters F1 and F2 applied; (c) Retrieved OCI/OC3 [*Chla*] against MODIS-A nFLH equiv. [*Chla*]; (d) Same as 10c but with filter F1 & F2 applied. The vertical line shows the NN [*Chla*] KB threshold (F2 mask) consistent with the existence of KB, residual pixels of F1 and F2 masks satisfy both maximum backscatter and minimum NN [*Chla*] and represent values for KB blooms. Color coding of the dots denotes distance to shore, with red being the closest.

Again, when the comparison between OCI/OC3 and MODIS-A NN retrieved [*Chla*] is expanded beyond area A to include all areas, including the more complex in-shore waters, the correlation between

them drops drastically, to $R^2 = 0.07$ (not shown) from the $R^2 = 0.75$ in Figure 10c for the off-shore area A. This may be due to the poorer retrievals associated with both nFLH and OCI/OC3 for more complex in-shore waters with increased backscatter [3,21,39–41,53,56].

3.2.4. Comparisons of VIIRS NN Retrievals with Red/Green Chlorophyll-*a* Index (RGCI) Retrievals

We next examine RGCI [*Chla*] retrievals for the same 2 September 2014 date and locations as in the above Sections. Equation (3a) below gives the relationship for RGCI MODIS-A [*Chla*] retrievals, and Equation (3b) that for RGCI VIIRS [*Chla*] retrievals [42].

$$[Chla]_{RGCI} = 0.1 \times \exp \left(11.8 \times \frac{Rrs667}{Rrs547} \right), \mu g L^{-1} \tag{3a}$$

$$[Chla]_{RGCI} = 0.1 \times \exp \left(11.8 \times \frac{Rrs671}{Rrs551} \right), \mu g L^{-1} \tag{3b}$$

We first compare VIIRS RGCI [*Chla*] retrievals against VIIRS NN [*Chla*] retrievals. Figure 11a shows a correlation of $R^2 = 0.72$ for open ocean area A. This drops to $R^2 = 0.49$ when filters F1 and F2 are applied, Figure 11b. This compares with $R^2 = 0.9$ and $R^2 = 0.78$ for the equivalent comparisons between OCI/OC3 and VIIRS NN [*Chla*].

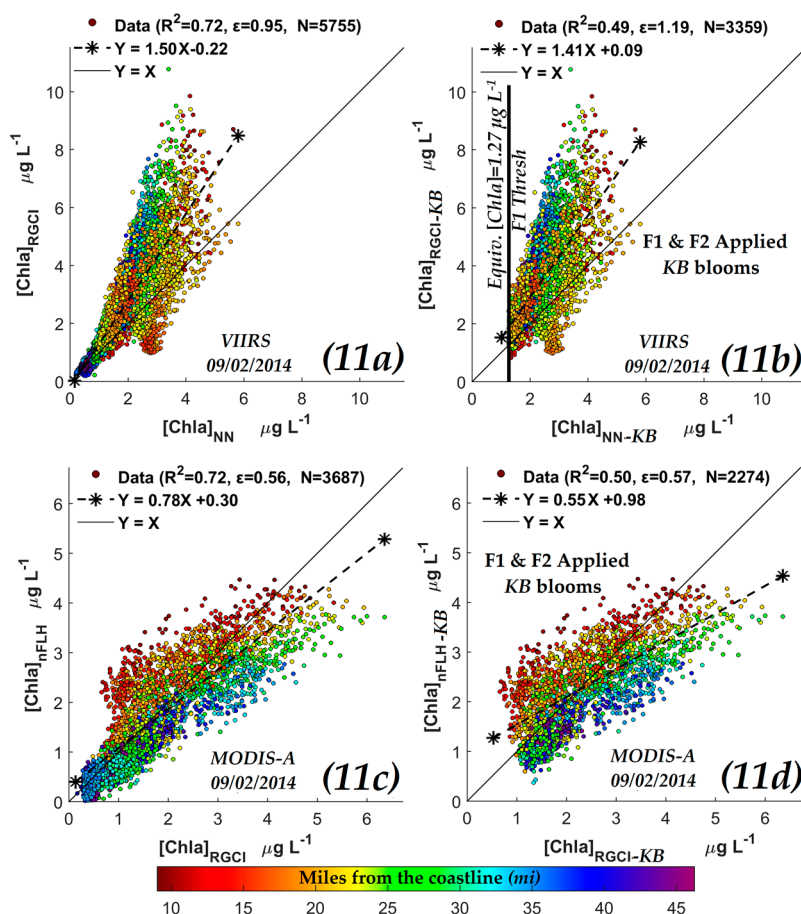


Figure 11. (a) Retrieved VIIRS RGCI [*Chla*] against retrieved VIIRS NN [*Chla*]; (b) Same retrieval as 11a with Filters F1 and F2 applied; (c) Retrieved RGCI [*Chla*] against MODIS-A nFLH equiv. [*Chla*]; (d) Same as 11c but with filter F1 & F2 applied. The vertical line shows the NN [*Chla*] KB threshold (F2 mask) Color coding of the dots denotes distance to shore, with red being the closest.

We next compare RGCI [*Chla*] against nFLH MODIS-A [*Chla*] retrievals. We see that for the same off shore area A, Figure 11c, $R^2 = 0.72$. This is lower than the $R^2 = 0.87$ obtained for the equivalent comparison of nFLH against MODIS-A NN [*Chla*] retrievals, Figure 7a, above. When the comparison is not restricted to the off-shore areas, the correlation for RGCI-nFLH drops off completely to $R^2 = 0.0$ (not shown) compared to the previously given equivalent correlations for nFLH-MODIS-A NN of $R^2 = 0.19$, Figure 8 and $R^2 = 0.07$ for OCI/OC3 (not shown).

When the F1 and F2 filtering procedures are applied to the RGCI [*Chla*] retrievals, for area A, the correlation against nFLH MODIS-A [*Chla*] retrievals drops to $R^2 = 0.50$, Figure 11d. This compares to $R^2 = 0.71$ and $R^2 = 0.50$ for the equivalent correlations, shown previously, between nFLH and MODIS-A NN and MODIS-A OCI/OC3 respectively.

The salient points of Sections 3.2.1–3.2.4 show that in open ocean area A, nFLH [*Chla*] retrievals from MODIS-A are well correlated with MODIS-A NN [*Chla*] retrievals $R^2 = 0.87$, less so with equivalent MODIS-A OCI/OC3 with $R^2 = 0.75$, and MODIS-A RGCI with $R^2 = 0.72$. All correlations drop when filters F1 and F2 are applied to obtain KB HABS retrievals to $R^2 = 0.71$, $R^2 = 0.5$ and $R^2 = 0.5$, respectively. For comparisons not restricted to the off-shore area A, all correlations with nFLH MODIS-A [*Chla*] retrievals drop off drastically to $R^2 = 0.19$, $R^2 = 0.07$ and $R^2 = 0.0$ for MODIS-A NN, MODIS-A OCI/OC3 and RGCI respectively. It should also be noted that all four retrieval techniques compared show qualitatively similar KB HABS retrieval images of the type shown in Figures 5a,b, 6b, and 9 (not shown for OCI/OC3 and RGCI).

3.3. Comparisons of VIIRS NN, OCI/OC3 and RGCI Retrievals with *in Situ* Cell Count Measurements

3.3.1. Evaluation of VIIRS KB HABS Retrievals against *in Situ* Measurement for Match-Ups Occurring over 2012–2015 Period

The ultimate test for the viability of KB HABS satellite retrieval techniques is their ability to match retrieved values with concurrent *in situ* measurements.

It is, however, difficult to find on any one day sufficient matches between satellite observations between concurrent, or near concurrent *in situ* measurements to obtain statistically meaningful results. We therefore extended the study period to look at all available WFS match-ups, Figure 12, between VIIRS measurements and *in situ* data at concurrent dates and over the 2012–2015 period for which there was available VIIRS data. The conditions for match-up were: (1) pixel centers were 0.3 miles or less from the *in situ* measurement location; pixels are excluded from the match-up comparison if they had been flagged for land, cloud, failure in atmospheric correction, stray light, bad navigation quality, both high and moderate glint, negative Rayleigh corrected radiance, viewing angle greater than 60, and solar zenith larger than 70, and any pixels which has water leaving radiance spectra with negative values in any one of its wavelengths. Cell counts sample measurements also had to be at less than 1 meter depth, and at concentrations $\geq 10^4$ cells \cdot L $^{-1}$. It should be noted that [*Chla*] of 1 μ g \cdot L $^{-1}$ is $\sim 10^5$ cells \cdot L $^{-1}$ [49].

The *in situ* cell count data was obtained from the Florida Fish and Wildlife Conservation Commission's Fish and Wildlife Research Institute (FWC-FWRI). The search for match-up between VIIRS satellite and *in situ* observations on the same day showed 94 cases which satisfied the match-up conditions specified above. Figure 13a, above, shows the relationship between NN retrieved a_{ph443} and the *in situ* KB cell measurements for these 94 cases. This shows a correlation with $R^2 = 0.32$. Converting the a_{ph443} [16] to equivalent [*Chla*] for these same 94 cases, shows, in Figure 13b, the same correlation against KB cell counts, with $R^2 = 0.32$ for both these match-ups. Figure 13c,d, show the equivalent match-up for the same 94 points for retrieved OCI/OC3 and RGCI [*Chla*] against *in situ* KB cell counts, which shows lower correlations with $R^2 = 0.28$ and $R^2 = 0.17$ respectively.

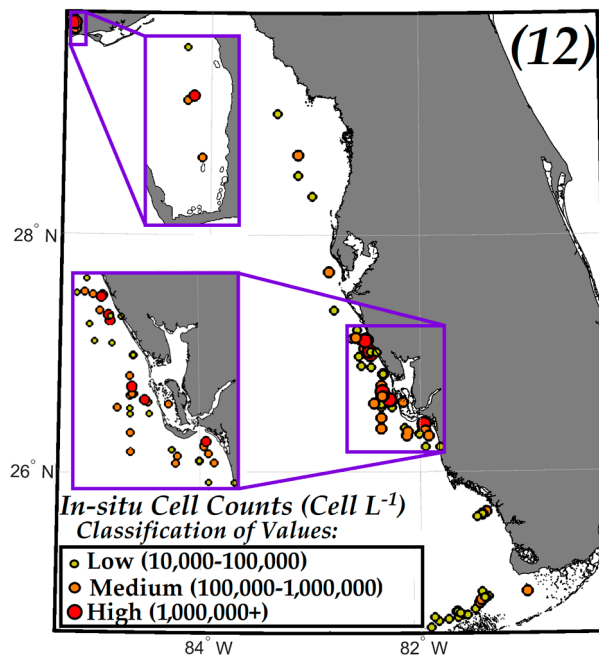


Figure 12. Showing *in situ* locations of *Karenia brevis* cell counts cover the range $0.01\text{--}9.2 \cdot 10^6$ cells $\cdot \text{L}^{-1}$ collected by Florida Fish and Wildlife Conservation Commission (FWC). Zoomed areas illustrate the extent of the underline details of *KB* values available in VIIRS retrievals for the period of 2012–2015.

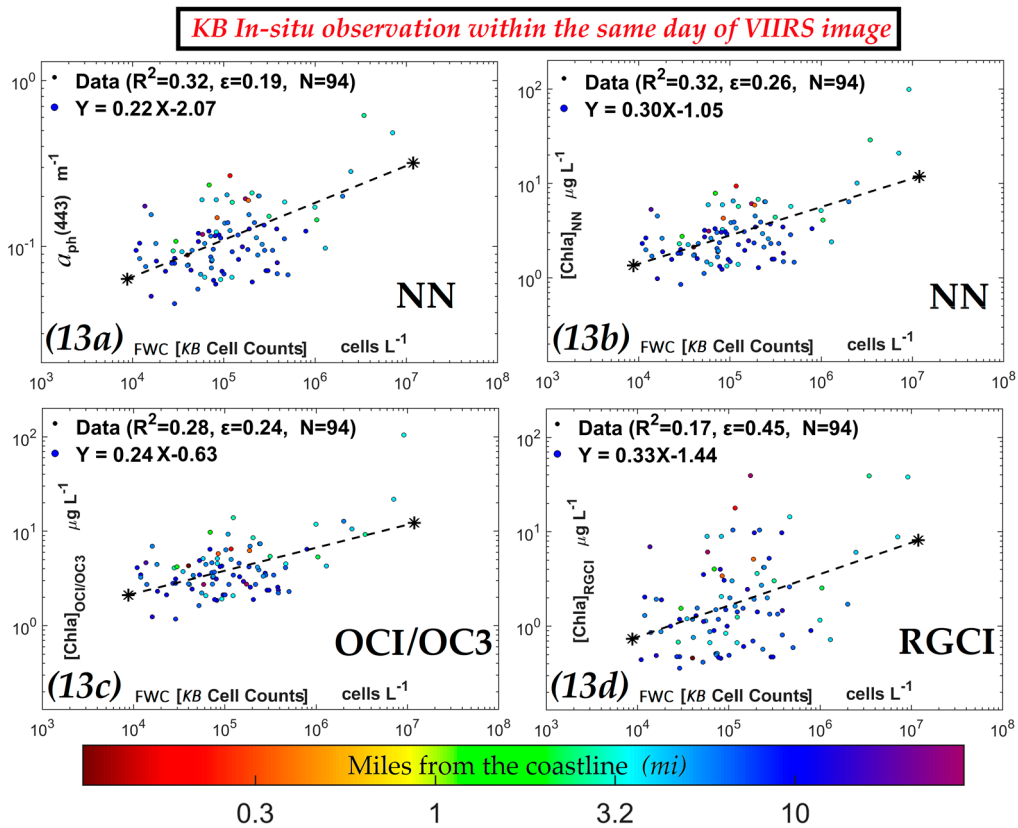


Figure 13. *In situ* observation within the same day of VIIRS image: (a) VIIRS NN retrieved a_{ph443} against *in situ* *KB* cell counts; (b) VIIRS NN equiv. $[Chla]$ against *in situ* cell counts; (c) VIIRS OCI/OC3 retrieved $[Chla]$ against *in situ* *KB* cell counts; (d) VIIRS RGC1 retrieved $[Chla]$ against *in situ* *KB* cell counts. Color coding of the dots denotes distance to shore, with blue being the closest.

Now, it is recognized that temporal variations due to bloom drift *etc.* between satellite observation and *in situ* measurement times can affect these results. Accordingly, the results were separated in accordance with observation time windows. Those occurring with less than 1 h, and 0.5 h between satellite and *in situ* observations are shown separately. Figure 14a (1 h), b (0.5 h) show the match-ups between VIIRS NN retrieved equivalent [Chla] against KB cell counts. The equivalent values for OCI/OC3 and RGCI [Chla] retrievals are shown in Figure 14c–f respectively. For the 1 h window, Figure 14a, the correlation for the NN retrievals increases from the daily $R^2 = 0.32$ to $R^2 = 0.69$. For OCI/OC3 retrievals, it increases from $R^2 = 0.28$ to $R^2 = 0.33$. For RGCI it increases from $R^2 = 0.17$ to $R^2 = 0.62$. For the 0.5 h window, the correlations increase to $R^2 = 0.82$, $R^2 = 0.44$ and $R^2 = 0.7$ respectively. With the NN being the highest, closely followed by RGCI, then OCI/OC3, though the average errors appear to be twice as high for RGCI as compared with NN.

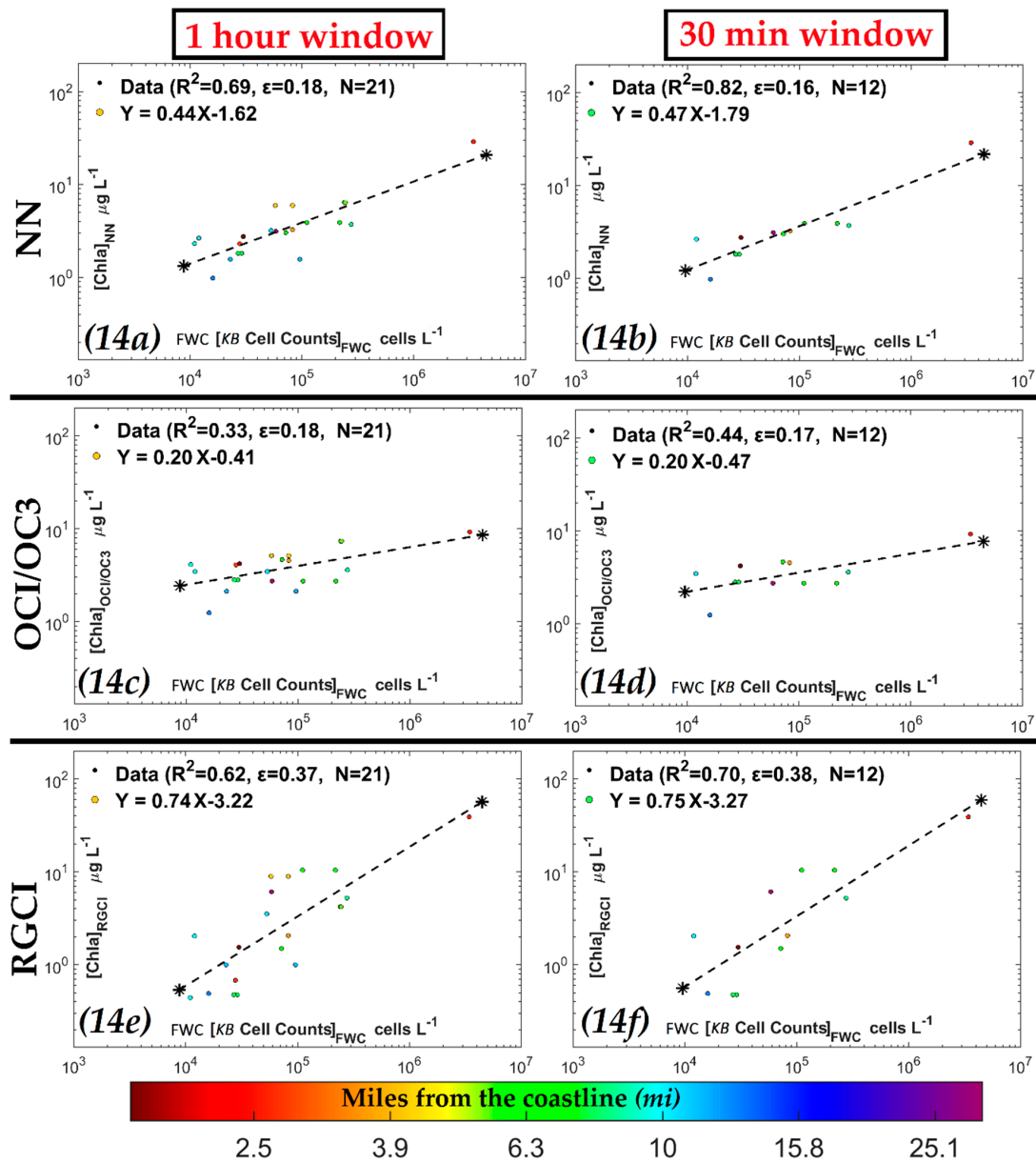


Figure 14. (a–f) Retrieved NN equiv. [Chla] and OCI/OC3 [Chla] and RGCI [Chla] against *in situ* cell counts for 1 h and 30 min observation time windows. Note that the vertical color bar is indicates distant (mi) from coastline with red being closest to shore.

Thus, it is seen that reducing the time window between satellite and *in situ* observations can generally significantly increase the correlation between VIIRS retrieved [Chla] and KB cell counts. More area specific studies need to be carried out before definitive conclusions can be drawn.

We also use the above match-ups to assess the validity of the F1 and F2 filter limits for $Rrs_{551} \leq 6.0 \times 10^{-3} \text{ sr}^{-1}$ and $a_{ph443} \geq 0.061 \text{ m}^{-1}$ defined in Section 3.1 above. Figure 15 shows that for the NN retrieved a_{ph443} match-ups falling within the 1/2 h window, which were retrieved without any filter constraints being applied on Rrs_{551} and a_{ph443} all but two of them fall within these limits. Further refinements on these limiting filter values as a means of retrieving KB HABs will require planned future statistical analysis of false positives and negatives in retrieval results against *in situ* measurements.

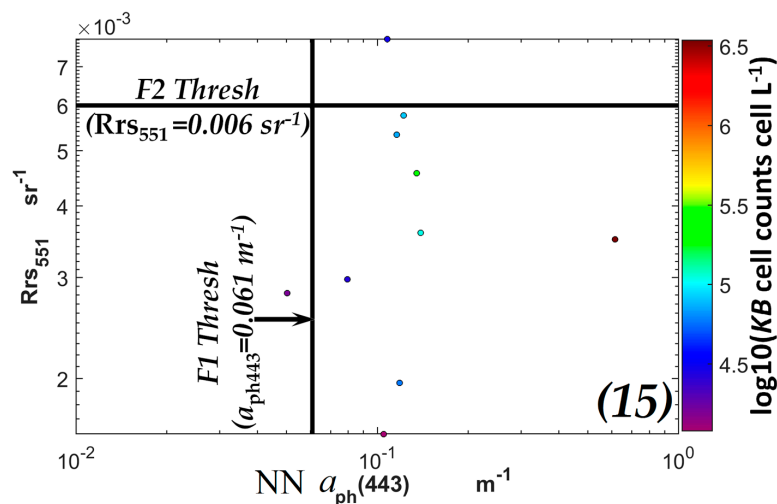


Figure 15. Shows the match-ups falling within the 1/2 h window, with both filter thresholds.

Table 1 below shows summary table of retrieval comparisons, *in situ* results and KB thresholds criteria applied.

Table 1. VIIRS, MODIS-A comparisons and *in situ* results.

y-axis		x-axis	R^2	Slope & Intercept	ϵ	N
OCI/OC3 [Chla] ($\mu\text{g}\cdot\text{L}^{-1}$)	VIIRS	NN-[Chla] ($\mu\text{g}\cdot\text{L}^{-1}$)	0.90	$y = 0.96x + 0.22$	0.33	5755
RGCI [Chla] ($\mu\text{g}\cdot\text{L}^{-1}$)			0.72	$y = 1.50x - 0.22$	0.95	5755
nFLH [Chla]-KB	MODIS	OCI/OC3 [Chla] ($\mu\text{g}\cdot\text{L}^{-1}$)	0.71	$y = 0.80x + 0.36$	0.43	2274
($W\cdot\text{m}^{-2}\cdot\mu\text{m}^{-1}\cdot\text{sr}^{-1}$)			0.50	$y = 0.48x + 0.70$	0.57	2274
RGCI [Chla] ($\mu\text{g}\cdot\text{L}^{-1}$)			0.50	$y = 0.55x + 0.98$	0.57	2274
NN [Chla] ($\mu\text{g}\cdot\text{L}^{-1}$)	In situ	KB Cell Counts (cells L^{-1}) Same day observations not restricted to open ocean areas	0.32		0.26	94
OCI/OC3 [Chla] ($\mu\text{g}\cdot\text{L}^{-1}$)			0.28		0.24	94
RGCI [Chla] ($\mu\text{g}\cdot\text{L}^{-1}$)			0.17		0.45	94
NN [Chla] ($\mu\text{g}\cdot\text{L}^{-1}$)	In situ	KB Cell Counts (cells L^{-1}) 1 h window	0.69		0.18	21
OCI/OC3 [Chla] ($\mu\text{g}\cdot\text{L}^{-1}$)			0.33		0.18	21
RGCI [Chla] ($\mu\text{g}\cdot\text{L}^{-1}$)			0.62		0.37	21
NN [Chla] ($\mu\text{g}\cdot\text{L}^{-1}$)	In situ	KB Cell Counts (cells L^{-1}) 30 min window	0.82		0.16	12
OCI/OC3 [Chla] ($\mu\text{g}\cdot\text{L}^{-1}$)			0.44		0.17	12
RGCI [Chla] ($\mu\text{g}\cdot\text{L}^{-1}$)			0.70		0.38	12

Criteria Applied in WFS for KB-HABs Retrievals

Rrs_{551}	NN a_{ph443}	Equivalent NN [Chla] Value
$\leq 0.006 \text{ sr}^{-1}$	$\geq 0.061 \text{ m}^{-1}$	$\geq 1.27 \mu\text{g L}^{-1}$

3.3.2. Evaluation of NN KB HABs Retrievals for Specific Bloom Events

We also compared the ability of NN KB HABs retrievals against *in situ* KB HABs measurements for specific algal blooms. We apply filter processes F1 and F2 above to VIIRS NN a_{ph443} retrievals to arrive at KB compatible values, in Figures 16 and 17a,b for three bloom dates: 28 August 2014, 16 November 2014 and 9 October 2012. The residual a_{ph443} (left hand scale) and equivalent [Chla] values (right hand scale) are those compatible with KB HABs. Figure 16 shows the retrievals for the 8 August 2014, bloom now overlaid with actual KB cell counts for that date only (not for a range of overlapping dates as was used previously). There are a total of 20 match-ups on that day. There appears to be one false positive, indicated by the arrow. This presents an ambiguous situation, since it is near the edge of the bloom and changes may have occurred in the time window between *in situ* and satellite measurement, and secondly, while there is no *in situ* bloom measured at the surface at that date, there was one below the surface at nearly the same location, bringing into play the possibility of sub-pixel variations, indistinguishable when pixel averaging takes place. Figure 17a shows a bloom on 16 November 2014, near the coast, with a total of 6 match-ups. There are no false positives or negatives in this retrieval. This is particularly interesting since it is close to the coast, and therefore in more complex waters. Figure 17b shows a bloom on 9 October 2012, with 12 match-ups. It covers both near and offshore areas and has no false positives or negatives.

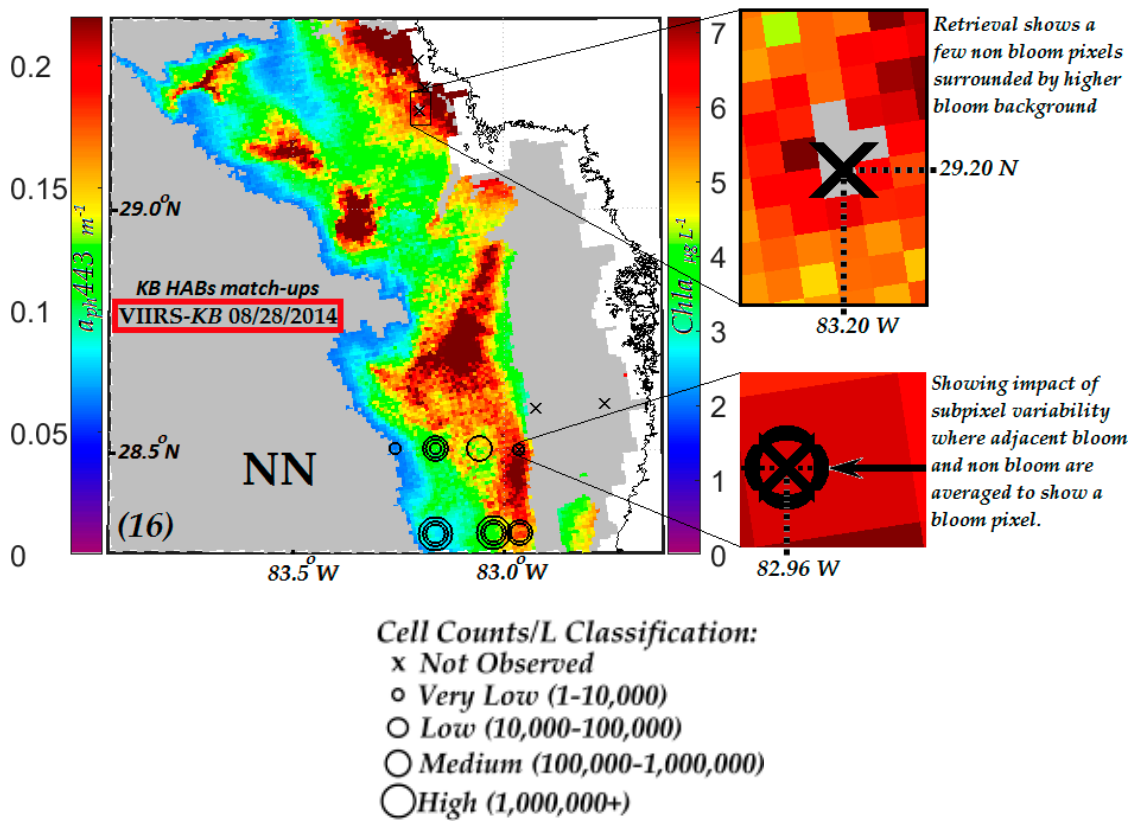


Figure 16. VIIRS-NN KB HABs retrievals for blooms date (28 August 2014), showing bloom compatible a_{ph443} and equiv. [Chla] values. Notes image are overlaid with cell counts for this date. White areas represent cloud cover or invalid data.

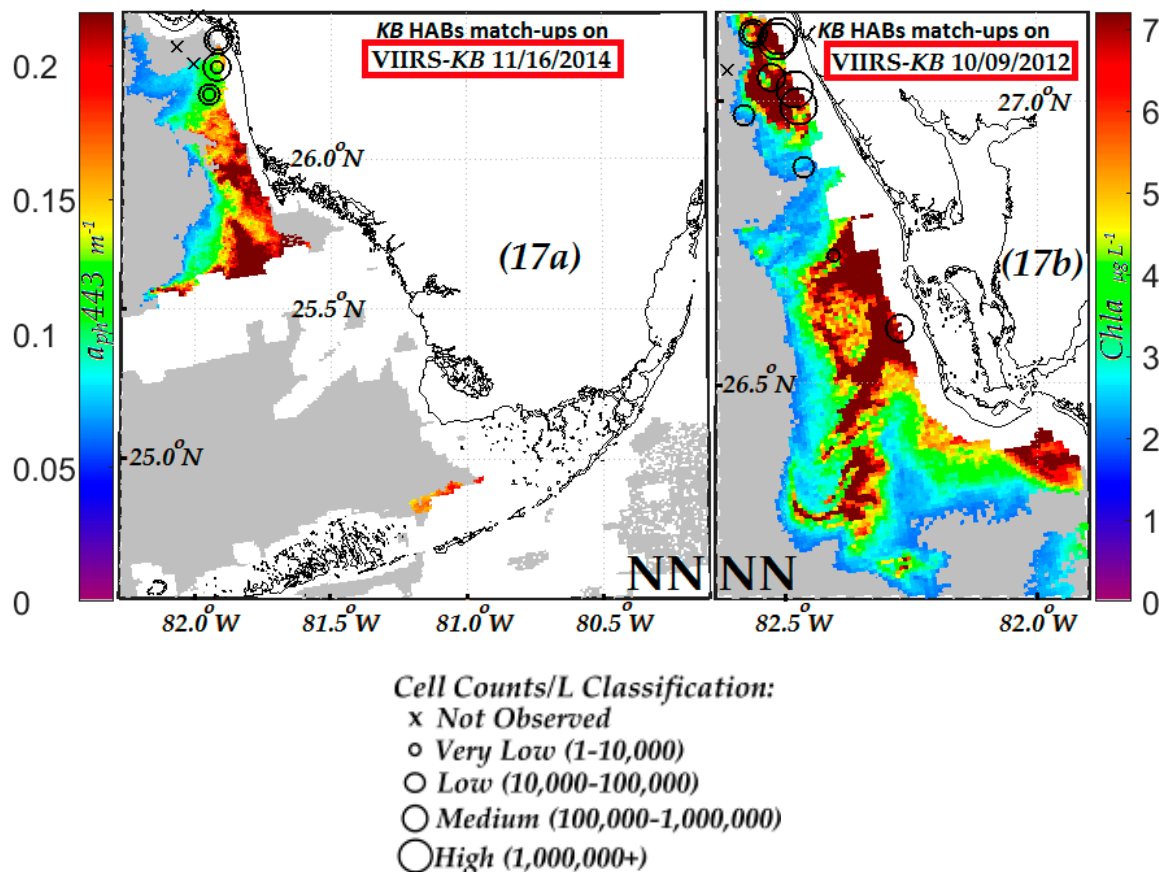


Figure 17. VIIRS-NN KB HABs retrievals on 2 different blooms dates, showing bloom compatible a_{ph443} and equiv. $[Chla]$ values. (a) 11 November 2014, bloom; (b) 09 October 2012, bloom. Notes all images are overlaid with cell counts corresponding for these dates. White areas represent cloud cover or invalid data.

4. Summary and Conclusions

Detection of KB HABs in the WFS have been aided in the past by use of the 678 nm MODIS-A fluorescence band for retrievals using nFLH and RBD techniques. The lack of a fluorescence channel on the successor VIIRS satellite provided the impetus for the NN work reported here. In this approach, NN algorithms using Rrs values from the 486, 551 and 671 nm VIIRS bands are used to retrieve an image of a_{ph443} values in the WFS. Then, as detailed above, the additional limiting constraints are applied, in two filter processes, F1 and F2 to eliminate from that image all a_{ph443} pixels which are not compatible with the existence of KB HABs. These limiting criteria are defined by (i) low backscatter manifested as a maximum VIIRS $Rrs551max$ value [3,17,18] and (ii) the minimum $[Chla]$ and hence equivalent minimum (a_{ph443}) values that are known to be associated with KB HABs in the WFS. Thus, through the implementation of filter processes F1 and F2, all pixels in the VIIRS NN retrieved a_{ph443} image that are incompatible with KB HABs are eliminated. The residual image then shows only retrieved a_{ph443} values and their equivalent $[Chla]$ values that are consistent with the existence of KB HABs. The specific limiting values for maximum $Rrs551$ and minimum a_{ph443} used in the filter processes were based on published data, reinforced and refined by inspections of retrieval results against available *in situ* data. The retrieved values of a_{ph443} and equivalent $[Chla]$ retrieved using these filter limits, were then compared both qualitatively and quantitatively both against other satellite retrieval techniques and *in situ* measurements.

Comparisons of the NN technique were made first with the nFLH and RBD techniques, which, in reported comprehensive tests [3] exhibited the best statistics for KB HABs retrievals in the WFS from

MODIS-A. Our comparisons showed good correlations between nFLH and the NN retrievals for open ocean waters. However, *KB* retrieval capabilities with the nFLH technique are severely limited for in-shore retrievals, where the more complex waters with increased non-algal particulate scattering interfere with the fluorescence signal making its interpretation more difficult [56]. Comparisons were also made between the NN technique and retrievals using OCI/OC3 and the RGCI for [*Chla*] retrievals. Again, these comparisons showed reasonable correlations in open ocean waters, but confirmed difficulties with retrievals in more complex inshore waters. Further work is also needed on our NN *KB* retrieval technique before we can properly evaluate its capabilities for in-shore retrieval and compare them more rigorously with those of MODIS-A nFLH, OCI/OC3 and RGCI.

Finally, the critical test for the viability of *KB* HABs satellite retrieval techniques is the comparison of their ability to match retrieved values with concurrent *in situ* measurements. We therefore sought to extend the range of available *in situ* comparisons. This was done by seeking all available match-ups between VIIRS NN a_{ph443} (and equivalent [*Chla*] retrievals) and *in situ* *KB* cell count measurements for the period 2012–2015. These comparisons showed that when the window between *in situ* observations and satellite measurements was reduced from daily, to 1 h and 0.5 h, the correlations greatly improved for the VIIRS NN and VIIRS RGCI retrievals against *in situ* match-ups. These showed respectable $R^2 = 0.82$ and $R^2 = 0.70$ respectively for the 0.5 h window. The comparisons also supported the choice of values for the F1 and F2 filter processes. Comparisons were also made comparing VIIRS NN retrievals identifying *KB* HABs, and *in situ* *KB* cell counts measured on the same date for 3 specific bloom events. All three confirmed the viability of the VIIRS NN retrieval approach, with no apparent false negatives or positives. Comparisons with other NN retrieval techniques are not so straightforward. Several of the previously reported NN techniques have used *in situ* measurements of IOPs, including sea surface temperatures and other physical parameters as inputs to NNs for bloom prediction, apparently with some success [57–59]. The more directly comparable NN technique reported, is the NN algorithm product for [*Chla*] retrievals in Case 2 waters [60–63] from the MERIS satellite, which is no longer operational. This appears to give comparable results, in European waters, to OCI/OC3 retrievals in open waters, and possibly higher accuracies in coastal waters [61]. This MERIS algorithm does not appear to have been tested for *KB* retrievals in the WFS. Tests of historical data for such retrievals may yield interesting results.

In conclusion, results to date with the VIIRS NN technique appear promising. However, more match-ups, including more detailed considerations of observation times and their connections to false positives or negatives, sample depths, distance to observation pixel centers and sub-pixel variability and impact of complex in-shore waters need to be studied. More comprehensive statistics need to be obtained on the overall efficacy of the approach and its comparisons to other techniques.

Acknowledgments: This work was partially supported by grants from NOAA through NOAA CREST, and NOAA JPSS. We would like to thank the NASA Ocean Color Processing Group for satellite imagery. We also thank NOAA HABSOS and Florida Fish and Wildlife Conservation Commission’s Fish and Wildlife Research Institute (FWRI) groups for making *in situ* *KB* data available to us.

Author Contributions: All authors contributed equally to this work.

Conflicts of Interest: The authors declare no conflict of interest.

Abbreviations

The following abbreviations are used in this manuscript:

<i>KB</i>	<i>Karenia brevis</i>
HABs	Harmful algal blooms
WFS	West Florida Shelf
VIIRS	Visible Infrared Imaging Radiometer Suite
MODIS-A	Moderate Resolution Imaging Spectroradiometer Aqua
MERIS	MEDium Resolution Imaging Spectrometer

a_{ph}	Absorption coefficient due to phytoplankton particulates (m^{-1})
a_{dg}	Absorption coefficient due to non-phytoplankton particulates and dissolved substances, $a_{dm} + a_g$ (m^{-1})
a_{dm}	Absorption coefficient due to non-phytoplankton particulates (m^{-1})
a_w	Absorption coefficient due to water (m^{-1})
a_t	Total absorption coefficient, $a_{ph} + a_{dm} + a_g + a_w$ (m^{-1})
b_{bp}	Backscattering coefficient due to particulates (m^{-1})
b_{bw}	Backscattering coefficient due to water (m^{-1})
b_b	Total backscattering coefficient, $b_{bp} + b_{bw}$ (m^{-1})
[Chla]	Chlorophyll- <i>a</i> concentration ($\mu g \cdot L^{-1}$)
CDOM	Color dissolved organic matter (ppm)
NAP	Non-phytoplankton particulate concentration ($g \cdot m^{-3}$)
AOP	Apparent optical properties
IOP	Inherent Optical properties
RT	Radiative transfer
Rrs	Above-surface remote-sensing reflectance (sr^{-1})
nLw	Normalized water leaving radiance ($W \cdot m^{-2} \cdot \mu m \cdot sr^{-1}$)
MLPNN	Multi Layer perceptron neural network
NN	Neural network
NN [Chla]	NN deriving [Chla] from Rrs as inputs
NOMAD	NASA bio-Optical Marine Algorithm Data set [21].
nFLH	normalized fluorescence height Algorithm [54].
OC	Ocean Color
OC3	Chlorophyll- <i>a</i> concentration ($\mu g \cdot L^{-1}$) derived using VIIRS and MODIS algorithm [39–41].
OCI	Chlorophyll- <i>a</i> concentration ($\mu g \cdot L^{-1}$) derived using VIIRS and MODIS algorithm [39].
RGCI	Red Green chlorophyll- <i>a</i> Index
ϵ	Estimate of the standard deviation of the error
N	Number of points
μ	Mean value
σ	standard deviation

Appendix A

A1. NN Algorithm Background and Directions for Implementation for a_{ph443} Retrieval

Note: The material in this Appendix is presented in a manner intended to help those readers less familiar with the use of Neural Networks. In the interest of completeness, some of the material presented here repeats parts of Section 2 above.

A.1.1. Background

In the work presented, we applied a synthetically trained NN algorithm previously developed and reported by us [12–15] to solve the inverse problem [19,20] of retrieving physical variables, including a_{ph443} from, VIIRS observations of Rrs 486, 551 and 671 nm in the WFS. A background summary is given here.

The essence of the approach is the use of a standard multiband NN inversion algorithm that takes VIIRS Rrs measurements at the 486, 551 and 671 nm bands as inputs, and produces as output the related Inherent Optical Properties (IOPs), namely: absorption coefficients of phytoplankton (a_{ph443}) dissolved organic matter (a_g) and non-algal particulates (a_{dm}) as well as the particulate backscatter coefficient, (b_{bp}) all at 443 nm. (As discussed in Section 2 above, it is only with the NN output of a_{ph443} that we are concerned with here).

A.1.2. Synthetic Dataset

For development of the algorithm, available measurement data from the NASA bio-Optical Marine Algorithm Data set [21], (NOMAD) was used as a basis for establishing a range of possible IOP parameters and examining potential relationships between them. The full range of parameters, applicable to oceanic and coastal waters, and the relationships established between them were used as inputs to a bio-optical model [14,22,23]. This model, Figure 1a, with four components: water, phytoplankton, colored dissolved organic matter (CDOM) and non-algal particulates (NAP) as inputs, was constructed to create a synthetic database consisting of 20,000 IOP combinations covering the entire observable range of IOP parameters. These IOPs were then used with a HydroLight based [36], parameterized forward model described in Lee *et al.*, 2002 [23], to generate corresponding sets of Rrs values at 486, 551 and 671 nm for VIIRS, and at 488, 555 and 667 nm for MODIS-A, associated with each of the 20,000 IOPs (and the related different combinations of the four components) [12–15]. The range and variability of IOPs used in our bio-optical modeling is well represented in the literature [22–35] and covers both case 1 and case 2 waters.

A.1.3. NN Training

50% (10,000) of these sets of Rrs and related IOPs were then used [12–15], to train a VIIRS NN. Figure 1b, to model the relationship between input Rrs values at the 486, 551 and 671 nm bands for VIIRS and the related IOPs a_{ph} , a_g , a_d , bb_p coefficients, all at 443 nm, which is at the peak of phytoplankton absorption spectrum, and thus exhibits most variation in natural waters, (and where a_g and a_d are mutually constrained through an empirically derived relationship based on a study of NOMAD values) [12–15,21]. Figure 1b shows the VIIRS NN Architecture used. It is a one-hidden-layer multilayer perceptron (MLP) with six neurons at the hidden layer. Since this architecture was able to model our problems well, we did not further explore how this relationship might be improved by increasing the number of neurons or layers.

A back propagation learning procedure among a statistically representative synthetic dataset, based on NOMAD parameters for off shore and coastal waters was used to retrieve a_{ph443} given the measured Rrs values at three VIIRS bands 486, 551 and 671 nm. By suitable training, the back propagation learning procedure estimates the underlying complex relationships between the inputs and outputs by retrieving the NN weighting parameters and biases using standard minimization procedures on the residual output errors [64–69].

A.1.4. Testing the NN

The VIIRS NN algorithm was tested and evaluated using several statistical indicators. This was done initially on half the simulated data-set not used in the training, then on field data from the NOMAD. Finally, it was also tested on data from our own field campaign in the Chesapeake Bay during 2013, which represented well the typical range of water optical properties and chlorophyll-*a* concentrations in coastal regions. Shown below are the retrievals that were obtained against our *in situ* field measurements.

Figure A1,2 show the values retrieved using the VIIRS NN algorithm with *in situ* radiometer field measurements [14], of Rrs at 486, 551 and 671 nm, plotted against the values of $a_{ph443} \text{ m}^{-1}$ (A1), and $bb_p(443) \text{ m}^{-1}$ (A2) measured by *in situ* WETLabs instrumentation [70]. These showed reasonably good correlations and demonstrated the potential efficacy of the VIIRS NN retrievals from *in situ* measured Rrs values that are not impacted by atmospheric and surface effects. It provided impetus for testing NN applications for VIIRS HAB retrievals in the WFS, provided atmospheric corrections are adequate to give correct VIIRS derived Rrs values at the 486, 551 and 671 nm bands.

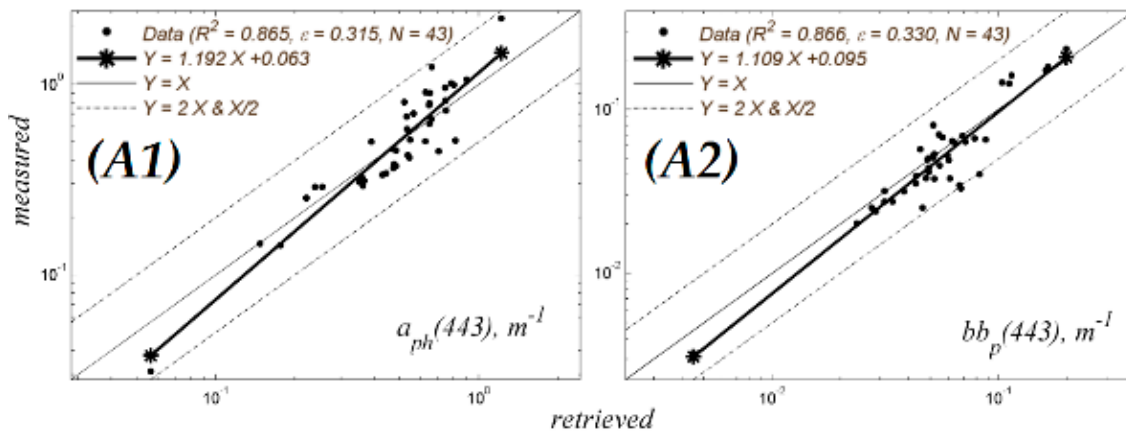


Figure A. (A1) Shows the retrieved a_{ph443} VIIRS NN; (A2) Shows the retrieved bb_{p443} VIIRS NN.

A2. Retrieval of a_{ph443} from $Rrs_{486, 551}$ and 671 nm Using NN

This section describes the steps required for the NN algorithm implementation, to be used for retrieving a_{ph443} from Rrs 486, 551 and 671 nm. The related calculations can be performed using a MATLAB script.

Data transformation and standardization: It should be noted that inputs of the NN were normalized and transformed into the log domain and standardized [69] by subtracting the mean and dividing by the standard deviation before the training stage. Therefore outputs need to be denormalized in the retrieval stage to obtain meaningful results.

The following steps shows NN a_{ph443} retrieval:

- I Retrieval of NN a_{ph443} in (m^{-1}) units, is obtained by denormalizing the NN output to obtain Equation (a1). below:

$$a_{ph443} = 10^{(\sigma_o \hat{a}_{ph443} + \mu_o)} \tag{a1}$$

where \hat{a}_{ph443} is the normalized phytoplankton absorption at 443 nm obtained by NN and carries out the final weighted sum activity and biases associated with the NN output $a_{ph443} m^{-1}$ and inputs Rrs_{486}, Rrs_{551} and Rrs_{671} nm shown below in (Equation (a3)). The μ_o (λ) and σ_o (λ) are the mean and standard deviation of the NN \hat{a}_{ph443} outputs respectively, obtained from the simulated datasets, and shown in Table A1.

- II Neural Network parameters needed for the above calculations:

The first step shown in (Equation (a2)) below, requires input reflectance's Rrs (λ), expressed as base 10 logarithm, standardized by removing, from each Rrs (λ), mean ($\mu_i(\lambda)$) of input values, of the simulated dataset, and then scaling the difference by the standard deviation ($\sigma_i(\lambda)$) of input values, of the simulated dataset, as shown in Equation (a2). Table A1 shows the relevant mean and standard deviation input (for each corresponding Rrs wavelength) and output values. (This procedure is also applied as the NN is trained using normalized Rrs (λ) values, so that it is equally sensitive to all inputs, avoiding conditioning problems).

Table A1. Mean and standard deviation of the NN trained Inputs and output.

	$\log_{10}(Rrs_{486})$	$\log_{10}(Rrs_{551})$	$\log_{10}(Rrs_{671})$		$\log_{10}(a_{ph443})$
μ_i	-2.2513	-2.4802	-3.4322	μ_o	-1.5257
σ_i	0.1862	0.3456	0.5904	σ_o	1.2596

The variable t , in the NN hyperbolic sigmoid activation function, $\left(\frac{2}{1+e^{-2t}} - 1\right)$ is used to transfer the weighted sum activity of each computational element (neuron), which carries out the final weighted sum activity and biases associated with the trained NN input, is given by Equation (a2).

$$t = \begin{bmatrix} -0.0026 & 0.7735 & 0.1217 \\ 0.6908 & -1.0168 & -0.3926 \\ 0.2805 & 0.4950 & -1.7261 \\ -0.4861 & 1.3790 & -0.7815 \\ -0.2008 & 0.4675 & -0.0311 \\ -0.0940 & -0.0076 & 0.0165 \end{bmatrix} * \left[\frac{\log_{10}(Rrs(\lambda_1)) - \mu_i(\lambda_1)}{\sigma_i(\lambda_1)}, \frac{\log_{10}(Rrs(\lambda_2)) - \mu_i(\lambda_2)}{\sigma_i(\lambda_2)}, \frac{\log_{10}(Rrs(\lambda_3)) - \mu_i(\lambda_3)}{\sigma_i(\lambda_3)} \right] + \begin{bmatrix} 2.2272 \\ -2.4660 \\ 2.4989 \\ -0.5527 \\ -0.2028 \\ 0.1321 \end{bmatrix} \quad (\text{a2})$$

\hat{a}_{ph443} is in turn related to t , by Equation (a3).

$$\hat{a}_{ph443} = \begin{bmatrix} 0.1410 & -0.6780 & -0.4435 & 0.0682 & 0.6546 & 0.3814 \\ -0.2470 & -0.8675 & -0.2453 & 0.0026 & 0.8058 & 0.6035 \\ 0.1087 & 0.2762 & -0.0687 & -0.9550 & 2.2780 & 0.6473 \\ 1.7204 & -0.0319 & -0.4128 & -0.1441 & 0.9679 & -1.2495 \end{bmatrix} * \left(\frac{2}{1+e^{-2t}} - 1\right) + \begin{bmatrix} -0.2646 \\ -0.2638 \\ 0.1398 \\ -1.0195 \end{bmatrix} \quad (\text{a3})$$

This will result in a specific value of \hat{a}_{ph443} for a set of $Rrs486$, $Rrs551$ and $Rrs671$ nm values. This value along with $\mu_o(\lambda)$ and $\sigma_o(\lambda)$ from Table A1 can now be used to complete evaluation of $a_{ph443} \text{ m}^{-1}$ Equation (a1).

References

- NOAA's National Ocean Service. Harmful Algal Blooms. Available online: <http://oceanservice.noaa.gov/hazards/hab> (accessed on 9 March 2015).
- Tomlinson, M.C.; Wynne, T.T.; Stumpf, R.P. An evaluation of remote sensing techniques for enhanced detection of the toxic dinoflagellate *Karenia brevis*. *Remote Sens. Environ.* **2009**, *113*, 598–609. [CrossRef]
- Soto, I.M.; Cannizzaro, J.; Muller-Karger, F.E.; Hu, C.; Wolny, J.; Goldgof, D. Evaluation and optimization of remote sensing techniques for detection of *Karenia brevis* blooms on the West Florida Shelf. *Remote Sens. Environ.* **2015**, *170*. [CrossRef]
- Soto-Ramos, I.M. Harmful Algal Blooms of the West Florida Shelf and Campeche Bank: Visualization and Quantification Using Remote Sensing Methods. Ph.D. Thesis, University of South Florida, Tampa, FL, USA, January 2013.
- Amin, R.; Gilerson, A.; Gross, B.; Moshary, F.; Ahmed, S. MODIS and MERIS detection of dinoflagellate blooms using the RBD technique. *Proc. SPIE* **2009**, *7473*, 747304.
- Amin, R.; Zhou, J.; Gilerson, A.; Gross, B.; Moshary, F.; Ahmed, S. Novel optical techniques for detecting and classifying toxic dinoflagellate *Karenia brevis* blooms using satellite imagery. *Opt. Express* **2009**, *17*, 9126–9144. [CrossRef] [PubMed]
- Hu, C.; Muller-Karger, F.E.; Taylor, C.; Carder, K.L.; Kelble, C.; Johns, E.; Heil, C.A. Red tide detection and tracing using MODIS fluorescence data: A regional example in SW Florida coastal waters. *Remote Sens. Environ.* **2005**, *97*, 311–321. [CrossRef]
- Hu, C.; Barnes, B.B.; Qi, L.; Corcoran, A.A. A harmful algal bloom of *Karenia brevis* in the Northeastern Gulf of Mexico as revealed by MODIS and VIIRS: A comparison. *Sensors* **2015**, *15*, 2873–2887. [CrossRef] [PubMed]
- Carvalho, G.A.; Minnett, P.J.; Banzon, V.F.; Baringer, W.; Heil, C.A. Long-term evaluation of three satellite ocean color algorithms for identifying harmful algal blooms (*Karenia brevis*) along the west coast of Florida: A matchup assessment. *Remote Sens. Environ.* **2011**, *115*, 1–18. [CrossRef] [PubMed]
- Carvalho, G.A.; Minnett, P.J.; Fleming, L.E.; Banzon, V.F.; Baringer, W. Satellite remote sensing of harmful algal blooms: A new multi-algorithm method for detecting the Florida Red Tide (*Karenia brevis*). *Harmful Algae* **2010**, *9*, 440–448. [CrossRef] [PubMed]
- Blondeau-Patissier, D.; Gower, J.F.; Dekker, A.G.; Phinn, S.R.; Brando, V.E. A review of ocean color remote sensing methods and statistical techniques for the detection, mapping and analysis of phytoplankton blooms in coastal and open oceans. *Progress Oceanogr.* **2014**, *123*, 123–144. [CrossRef]

12. Ioannou, I.; Gilerson, A.; Gross, B.; Moshary, F.; Ahmed, S. Neural network approach to retrieve the inherent optical properties of the ocean from observations of MODIS. *Appl. Opt.* **2011**, *50*, 3168–3186. [[CrossRef](#)] [[PubMed](#)]
13. Ioannou, I.; Gilerson, A.; Gross, B.; Moshary, F.; Ahmed, S. Deriving ocean color products using neural networks. *Remote Sens. Environ.* **2013**, *134*, 78–91. [[CrossRef](#)]
14. Ioannou, I.; Gilerson, A.; Ondrusek, M.; Hlaing, S.; Foster, R.; El-Habashi, A.; Bastani, K.; Ahmed, S. Remote estimation of in water constituents in coastal waters using neural networks. *Proc. SPIE* **2014**, 9240. [[CrossRef](#)]
15. El-habashi, A.; Ahmed, S. Neural network algorithms for retrieval of harmful algal blooms in the west Florida shelf from VIIRS satellite observations and comparisons with other techniques, without the need for a fluorescence channel. *Proc. SPIE* **2015**. [[CrossRef](#)]
16. Le, C.; Hu, C. A hybrid approach to estimate chromophoric dissolved organic matter in turbid estuaries from satellite measurements: A case study for Tampa Bay. *Opt. Express* **2013**, *21*, 18849–18871. [[CrossRef](#)] [[PubMed](#)]
17. Cannizzaro, J.P.; Carder, K.L.; Chen, F.R.; Heil, C.A.; Vargo, G.A. A novel technique for detection of the toxic dinoflagellate, *Karenia brevis*, in the Gulf of Mexico from remotely sensed ocean color data. *Cont. Shelf Res.* **2008**, *28*, 137–158. [[CrossRef](#)]
18. Cannizzaro, J.P.; Hu, C.; English, D.C.; Carder, K.L.; Heil, C.A.; Müller-Karger, F.E. Detection of *Karenia brevis* blooms on the west Florida shelf using *in situ* backscattering and fluorescence data. *Harmful Algae* **2009**, *8*, 898–909. [[CrossRef](#)]
19. Aires, F.; Prigent, C.; Rossow, W.B.; Rothstein, M. A neural network approach including first guess for retrieval of atmospheric water vapor, cloud liquid water path, surface temperature, and emissivities over land from satellite microwave observations. *J. Geophys. Res.* **2001**, *106*, 14887–14907. [[CrossRef](#)]
20. Aires, F.; Prigent, C.; Rossow, W.B. Neural network uncertainty assessment using Bayesian statistics: A remote sensing application. *Neural Comput.* **2004**, *16*, 2415–2458. [[CrossRef](#)] [[PubMed](#)]
21. Werdell, P.J.; Bailey, S.W. An improved *in situ* bio-optical data set for ocean color algorithm development and satellite data product validation. *Remote Sens. Environ.* **2005**, *98*, 122–140. [[CrossRef](#)]
22. IOCCG. *Remote Sensing of Inherent Optical Properties: Fundamentals, Tests of Algorithms, and Applications*; Report 5; Lee, Z.-P., Ed.; IOCCG: Bay Saint Louis, MS, USA, 2006; pp. 57–62.
23. Lee, Z.P.; Carder, K.L.; Arnone, R.A. Deriving inherent optical properties from water color: A multiband quasi-analytical algorithm for optically deep waters. *Appl. Opt.* **2002**, *41*, 5755–5772. [[CrossRef](#)] [[PubMed](#)]
24. Morel, A. Optical modeling of the upper ocean in relation to its biogenous matter content (case I waters). *J. Geophys. Res.* **1988**, *93*, 10749–10768. [[CrossRef](#)]
25. Gordon, H.R.; Brown, O.B.; Evans, R.H.; Brown, J.W.; Smith, R.C.; Baker, K.S.; Clark, D.K. A semi-analytic radiance model of ocean color. *J. Geophys. Res.* **1988**, *93*, 10909–10924. [[CrossRef](#)]
26. Morel, A.; Maritorena, S. Bio-optical properties of oceanic waters: A reappraisal. *J. Geophys. Res.* **2001**, *106*, 7163–7180. [[CrossRef](#)]
27. Lee, Z.P. International Ocean-Colour Coordinating Group. Available online: http://www.ioccg.org/groups/lee_data.pdf (accessed on 9 March 2015).
28. Bricaud, A.; Babin, M.; Morel, A.; Claustre, H. Variability in the chlorophyll-specific absorption coefficients of natural phytoplankton: Analysis and parameterization. *J. Geophys. Res.* **1995**, *100*, 13321–13332. [[CrossRef](#)]
29. Bukata, R.P.; Jerome, J.H.; Kondratyev, K.Y.; Pozdnyakov, D.V. *Optical Properties and Remote Sensing of Inland and Coastal Waters*; CRC Press: Boca Raton, FL, USA, 1995.
30. Stramski, D.; Bricaud, A.; Morel, A. Modeling the inherent optical properties of the ocean based on the detailed composition of the planktonic community. *Appl. Opt.* **2001**, *40*, 2929–2945. [[CrossRef](#)] [[PubMed](#)]
31. Pope, R.; Fry, E. Absorption spectrum 380–700 nm of pure waters: II. Integrating cavity measurements. *Appl. Opt.* **1997**, *36*, 8710–8723. [[CrossRef](#)] [[PubMed](#)]
32. Morel, A. Optical properties of pure water and pure sea water. In *Optical Aspects of Oceanography*; Jerlov, N.G., Nielsen, E.S., Eds.; Academic Press: New York, NY, USA, 1974; pp. 1–24.
33. Ciotti, A.M.; Lewis, M.R.; Cullen, J.J. Assessment of the relationships between dominant cell size in natural phytoplankton communities and the spectral shape of the absorption coefficient. *Limnol. Oceanogr.* **2002**, *47*, 404–417. [[CrossRef](#)]
34. Mobley, C.D. *Light and Water: Radiative Transfer in Natural Waters*; Academic Press: New York, NY, USA, 1994.

35. Babin, M.; Morel, A.; Fournier-Sicre, V.; Fell, F.; Stramski, D. Light scattering properties of marine particles in coastal and oceanic waters as related to the particle mass concentration. *Limnol. Oceanogr.* **2003**, *48*, 843–859. [[CrossRef](#)]
36. Mobley, C.D.; Sundman, L.K. *HYDROLIGHT 4.2*; Sequoia Scientific, Inc.: Bellevue, WA, USA, 2001.
37. Matthew Dornback. Harmful Algal Blooms Observing System. Available online: <http://habsos.noaa.gov/> (accessed on 9 March 2015).
38. NASA Ocean Biology (OB). *Suomi-NPP Visible Infrared Imaging/Radiometer Suite (VIIRS) and Moderate Resolution Imaging Spectroradiometer (MODIS-Aqua) Ocean Color Data*; NASA OB.DAAC: Greenbelt, MD, USA, 2014.
39. Hu, C.; Lee, Z.; Franz, B. Chlorophyll *a* algorithms for oligotrophic oceans: A novel approach based on three-band reflectance difference. *J. Geophys. Res.* **2012**, *117*. [[CrossRef](#)]
40. O'Reilly, J.E.; Maritorena, S.; O'Brien, M.C.; Siegel, D.A.; Toole, D.; Menzies, D.; Smith, R.C.; Mueller, J.L.; Mitchell, B.G.; Kahru, M.; *et al.* *SeaWiFS Postlaunch Calibration and Validation Analyses*; Part 3; Hooker, S.B., Firestone, E.R., Eds.; NASA Goddard Space Flight Center: Hampton, VA, USA, 2000; p. 49.
41. O'Reilly, J.E.; Maritorena, S.; Mitchell, B.G.; Siegel, D.A.; Carder, K.L.; Garver, S.A.; Kahru, M.; McClain, C.R. Ocean color chlorophyll algorithms for SeaWiFS. *J. Geophys. Res.* **1998**, *103*. [[CrossRef](#)]
42. Qi, L.; Hu, C.; Cannizzaro, J.; Corcoran, A.A.; English, D.; Le, C. VIIRS observations of a *Karenia brevis* bloom in the northeastern gulf of Mexico in the absence of a fluorescence band. *IEEE Geosci. Remote Sens. Lett.* **2015**, *12*, 2213–2217. [[CrossRef](#)]
43. Stumpf, R.P.; Tomlinson, M.C.; Calkins, J.A.; Kirkpatrick, B.; Fisher, K.; Nierenberg, K.; Currier, R.; Wynne, T.T. Skill assessment for an operational algal bloom forecast system. *J. Mar. Syst.* **2009**, *76*, 151–161. [[CrossRef](#)] [[PubMed](#)]
44. Tester, P.A.; Shea, D.; Kibler, S.R.; Varnam, S.M.; Black, M.D.; Litaker, R.W. Relationships among water column toxins, cell abundance and chlorophyll-*a* concentrations during *Karenia brevis* blooms. *Cont. Shelf Res.* **2008**, *28*, 59–72. [[CrossRef](#)]
45. Craig, S.E.; Lohrenz, S.E.; Lee, Z.; Mahoney, K.L.; Kirkpatrick, G.J.; Schofield, O.M.; Steward, R.G. Use of hyperspectral remote sensing reflectance for detection and assessment of the harmful alga, *Karenia brevis*. *Appl. Opt.* **2006**, *45*, 5414–5425. [[CrossRef](#)] [[PubMed](#)]
46. Stumpf, R.P.; Tomlinson, M.C. Remote sensing of harmful algal blooms. In *Remote Sensing of Coastal Aquatic Environments*; Miller, R.L., Del Castillo, C.E., McKee, B.A., Eds.; Springer: Dordrecht, The Netherlands, 2005; pp. 277–296.
47. Wynne, T.T.; Stumpf, R.P.; Tomlinson, M.C.; Ransibrahmanakul, V.; Villareal, T.A. Detecting *Karenia brevis* blooms and algal resuspension in the western Gulf of Mexico with satellite ocean color imagery. *Harmful Algae* **2005**, *4*, 992–1003. [[CrossRef](#)]
48. Tomlinson, M.C.; Stumpf, R.P.; Ransibrahmanakul, V.; Truby, E.W.; Kirkpatrick, G.J.; Pederson, B.A.; Vargo, G.A.; Heil, C.A. Evaluation of the use of SeaWiFS imagery for detecting *Karenia brevis* harmful algal blooms in the eastern Gulf of Mexico. *Remote Sens. Environ.* **2004**, *91*, 293–303. [[CrossRef](#)]
49. Stumpf, R.P.; Culver, M.E.; Tester, P.A.; Tomlinson, M.; Kirkpatrick, G.J.; Pederson, B.A.; Truby, E.; Ransibrahmanakul, V.; Soracco, M. Monitoring *Karenia brevis* blooms in the Gulf of Mexico using satellite ocean color imagery and other data. *Harmful Algae* **2003**, *2*, 147–160. [[CrossRef](#)]
50. Mahoney, K.L. backscattering of Light by *Karenia Brevis* and Implications for Optical Detection and Monitoring. Available online: http://aquila.usm.edu/theses_dissertations/3545/ (accessed on 9 March 2015).
51. Stumpf, R.P. Applications of satellite ocean color sensors for monitoring and predicting harmful algal blooms. *Hum. Ecol. Risk Assess. Int. J.* **2001**, *7*, 1363–1368. [[CrossRef](#)]
52. Carder, K.; Steward, R.G. A remote-sensing reflectance model of a red-tide dinoflagellate off west Florida. *Limnol. Oceanogr.* **1985**, *30*, 286–298. [[CrossRef](#)]
53. NASA's OceanColor Web by the Ocean Biology Processing Group (OBPG) at NASA's Goddard Space Flight Center. Available online: http://oceancolor.gsfc.nasa.gov/cms/atbd/chlor_a/ (accessed on 9 March 2015).
54. Behrenfeld, M.J.; Westberry, T.K.; Boss, E.S.; O'Malley, R.T.; Siegel, D.A.; Wiggert, J.D.; Franz, B.A.; McClain, C.R.; Feldman, G.C.; Doney, S.C.; *et al.* Satellite-detected fluorescence reveals global physiology of ocean phytoplankton. *Biogeosciences* **2009**, *6*, 779–795. [[CrossRef](#)]

55. Letelier, R.M.; Abbott, M.R. An analysis of chlorophyll fluorescence algorithms for the Moderate Resolution Imaging Spectrometer (MODIS). *Remote Sens. Environ.* **1996**, *58*, 215–223. [[CrossRef](#)]
56. Gilerson, A.; Zhou, J.; Hlaing, S.; Ioannou, I.; Schalles, J.; Gross, B.; Moshary, F.; Ahmed, S. Fluorescence component in the reflectance spectra from coastal waters. Dependence on water composition. *Opt. Express* **2007**, *15*, 15702–15721. [[CrossRef](#)] [[PubMed](#)]
57. Zhang, T.; Fell, F.; Liu, Z.S.; Preusker, R.; Fischer, J.; He, M.X. Evaluating the performance of artificial neural network techniques for pigment retrieval from ocean color in Case I waters. *J. Geophys. Res. Oceans* **2003**, *108*. [[CrossRef](#)]
58. Gross, L.; Thiria, S.; Frouin, R.; Mitchell, B.G. Artificial neural networks for modeling the transfer function between marine reflectance and phytoplankton pigment concentration. *J. Geophys. Res.* **2000**, *105*, 3483–3495. [[CrossRef](#)]
59. Matthews, M.W.; Bernard, S.; Winter, K. Remote sensing of cyanobacteria-dominant algal blooms and water quality parameters in Zeekoevlei, a small hypertrophic lake, using MERIS. *Remote Sens. Environ.* **2010**, *114*, 2070–2087. [[CrossRef](#)]
60. Schiller, H.; Doerffer, R. Neural network for emulation of an inverse model operational derivation of Case II water properties from MERIS data. *Int. J. Remote Sens.* **1999**, *20*, 1735–1746. [[CrossRef](#)]
61. Doerffer, R.; Schiller, H.; Krasemann, H. *MERIS Case 2 Water Validation Early Results North Sea/Helgoland/German Bight*; ESA Special Publication: Paris, France, 2003; p. 99.
62. Schiller, H.; Doerffer, R. Improved determination of coastal water constituent concentrations from MERIS data. *IEEE Trans. Geosci. Remote Sens.* **2005**, *43*, 1585–1591. [[CrossRef](#)]
63. Park, Y.J.; Ruddick, K. Detecting Algae Blooms in EUROPEAN Waters. In *ENVISAT Symposium*; European Space Agency Special Publication SP-636: Paris, France, 2007; pp. 23–27.
64. Bishop, C.M. *Neural Networks for Pattern Recognition*; Oxford University Press: Oxford, UK, 1995.
65. Levenberg, K. A method for the solution of certain non-linear problems in least squares. *Q. Appl. Math.* **1944**, *2*, 164–168.
66. Foresee, F.D.; Hagan, M.T. Gauss-Newton approximation to Bayesian regularization. IEEE International Joint Conference on Neural Networks: Houston, TX, USA, 1997.
67. Mackay, D.J.C. Bayesian interpolation. *Neural Comput.* **1992**, *4*, 415–447. [[CrossRef](#)]
68. Marquardt, D.W. An algorithm for the least-squares estimation of nonlinear parameters. *SIAM J. Appl. Math.* **1963**, *11*, 431–441. [[CrossRef](#)]
69. Lawrence, J. Data preparation for a neural network. *AI Expert* **1991**, *6*, 34–41.
70. Zaneveld, J.R.V.; Moore, C.; Barnard, A.H.; Walsh, I. Correction and analysis of spectral absorption data taken with the WET Labs ac-s. In *Proceedings of the Ocean Optics XVII, Perth, Australia, 25–29 October 2004*; pp. 25–29.

